frontiers in Marine Science

ORIGINAL RESEARCH
published: 29 October 2020
doi: 10.3389/fmars.2020.538675

Hydrodynamic Drivers and Morphological Responses on Small Coral Islands—The Thoondu Spit on Fuvahmulah, the Maldives

C. Gabriel David and Torsten Schlurmann*

Faculty of Civil Engineering and Geodetic Sciences, Ludwig-Franzius-Institute for Hydraulic, Estuarine and Coastal Engineering, Leibniz University Hannover, Hannover, Germany

Assessing the resilience of islands toward altered ocean climate pressures and providing robust adaptation measures requires an understanding of the interaction between morphological processes and the underlying hydrodynamic drivers. In this sense, this study presents changing sediment volumes on various temporal scales for the fringing reef island Fuvahmulah. Based on three field campaigns, conducted over 2 years, aerial imagery provides information on marine aggregates of the island's beaches. In addition, high resolution climate reanalysis data serves as input into an empirical and a numerical approach. Together, both approaches describe the driving processes behind volumetric seasonal and interannual changes: On the one hand, the empirical method quantifies sediment transport rates for calcareous sediments over the whole time span of the data set by considering wind and swell waves from multiple directions. On the other hand, the numerical method gives insights into the complexity of currents induced by dominant wave components. Combining these methods facilitates hindcasting and predicting morphological changes under varying wave climate, assessing sediment pathways over the whole reef, and describing the seasonal and interannual evolution of the sand spit Thoondu. As a result, this study reveals sediment distribution on different spatio-temporal scales and elucidates their significance in the design of conventional and alternative low-regret coastal adaptation.

Keywords: low-lying islands, morphology, coral reefs, global climate data, sand spit, Maldives, coastal management, climate change adaptation

OPEN ACCESS

Edited by:
Curt D. Storlazzi, United States Geological Survey (USGS), United States

Reviewed by:
Matthew John Eliot, Seashore Engineering, Australia
Peng Yao, Hohai University, China

****Correspondence:***
C. Gabriel David
david@lufi.uni-hannover.de

Specialty section:
This article was submitted to Coastal Ocean Processes, a section of the journal Frontiers in Marine Science

Received: *28 February 2020*
Accepted: *29 September 2020*
Published: *29 October 2020*

Citation:
David CG and Schlurmann T (2020) Hydrodynamic Drivers and Morphological Responses on Small Coral Islands—The Thoondu Spit on Fuvahmulah, the Maldives. Front. Mar. Sci. 7:538675. doi: 10.3389/fmars.2020.538675

1. INTRODUCTION

Small islands and atolls are exposed to sea level rise and associated impacts, as they lie only a few meters above mean sea level, while being fully surrounded by water. Thus, the fifth assessment report of the Intergovernmental Panel on Climate Change (IPCC) came to the conclusion that communities of small islands are particularly vulnerable to these impacts due to their inherent lack of means for retreat (Nurse et al., 2014). The Special Report Ocean and Cryosphere (SROCC) of the IPCC further finds that coastal risks for low-lying areas will increase, historically rare extreme sea level events will become common by 2100 under all climate change projection pathways, and that there are limits to any coastal protection within the current or following century (Oppenheimer et al., in press). Over a time span of decades, this could translate to uninhabitable atolls, as global

warming will be accompanied by stronger and more frequent sea-borne hazards (Storlazzi et al., 2015, 2018).

Reef islands are mainly vulnerable to shoreline erosion, inundation (including overwash), and saline intrusion (Nurse et al., 2014). These impacts are triggered by storm events and the rising sea levels (Ferrario et al., 2014). Tropical storms develop, among other factors, above a sea-surface temperature (SST) threshold of 27 °C (Tory and Frank, 2010). Thus, the frequency as well as intensity of tropical cyclones will increase within the 20° band around the equator in the face of global warming (Emanuel, 1988).

With climate change induced warming, reefs are more susceptible to coral bleaching. Therefore, higher water temperatures affect coral health directly (Pisapia et al., 2019). Corals are important for the livelihood of the accommodated reef islands. The reef is the major contributor of wave attenuation and thus protection of the inhabited island (Ferrario et al., 2014; Harris et al., 2018), because healthy coral reefs serve as natural buffers to shelter susceptible small coral islands from direct wave attack and consequent erosion (Narayan et al., 2016; Oppenheimer et al., in press). An ongoing increase of water levels in the face of climate change implies coral reefs might reach their biophysical limit of ecosystem-based protection within this century (Oppenheimer et al., in press).

But observations have shown that shorelines of reef islands respond individually to sea level rise impacts: while on the Solomon islands, severe shoreline recession and disappearing islands have been registered (Albert et al., 2016), net land area changes vary for other islands in the central and western Pacific, including positive sediment budgets despite sea level rise (McLean and Kench, 2015). Other coral reef islands have even formed and developed naturally during higher sea levels than the current mean sea level (East et al., 2018). This shows that sediment erosion and accretion is highly site specific and is sensitive to multiple drivers. However, the evolution of reef islands and their natural response to changing impacts mainly depend on the reef's individual sediment production rate and the sediment distribution under the given hydrodynamic circumstances:

Coral reefs serve as sediment source for the islands they inhabit (Woodroffe et al., 1999; Ryan et al., 2019)—sediment production rates depend on coral type (Hamylton et al., 2017), sea level (Perry et al., 2011), and location of the organisms on the reef (Ryan et al., 2019). Supply rates also vary over time, due to changes in reef growth, reef ecology and climate-driven perturbations, such as ocean acidification or increasing water temperature (Andersson, 2015; Kench and Mann, 2017; Perry et al., 2018).

On the other hand, sediment entrainment, transport and (re-)distribution on the reef is generally governed by swell waves, even though wind-waves can have an influence on flow patterns occasionally (Pomeroy et al., 2015, 2018). The island's shape and location on the reef depends on the incoming waves, the reef platform (Mandlier and Kench, 2012; Kench and Mann, 2017) as well as the island's orientation toward the dominant wave direction (Shope and Storlazzi, 2019).

The high morphologic activity allows reef islands to respond dynamically to natural ocean-climate pressures. However, coastal management efforts and infrastructure development often interfere with the inherent natural processes (Kench, 2012; David et al., 2019) adding to anthropogenic ocean-climate pressures (Duvat and Magnan, 2019) instead of providing appropriate and sustainable protection of lives, livelihoods and natural environments. In contrast, a "low-regret approach" would maintain the system's abilities and support it where and when adequate. According to the IPCC (2012), low-regret measures are concepts to manage the risks of extreme events and disasters, while offering (co-)benefits to the coastal community regardless of the current or future climate scenarios. Following a so-called *"working with nature"* or *"eco-system based"* approach (Stive et al., 2013; Temmerman et al., 2013; Tessler et al., 2015), candidates for sustainable low-regret measures include sea grass stabilization to prevent erosion (Möller et al., 2014; Paul and Gillis, 2015), bio-rock materials to mimic eco-friendly artificial reefs (David et al., 2016) or large scale artificial sand deposits, being naturally distributed by tides, waves and wind force toward beaches and dunes (Stive et al., 2013). But implementing sustainable climate change adaptation measures requires understanding natural and anthropogenic ocean-climate pressures, their impacts, the subsequent response, and the underlying processes—in the case of this study with regard to the reef. Applying this knowledge limits deteriorating impacts on ecosystems and associated ecosystem services, enables tailoring appropriate coastal protection solutions to the local conditions (Schoonees et al., 2019), and thus providing low-regret solutions.

In this study, we focus on the Maldivian island Fuvahmulah in the Indian Ocean. The Maldivian islands are susceptible to increased coral bleaching (Pisapia et al., 2019; Ryan et al., 2019; Skirving et al., 2019) and Fuvahmulah is a projected hotspot for sea level rise (Dangendorf et al., 2019). In addition, storms, storm surges, and occasional tsunamis commonly batter the coasts of the Maldives as any low-lying small islands (Nurse et al., 2014). With its location close to the equator and in between the Indian Ocean Dipole (IOD), the island is also prone to experience SST-based increase of cyclone activity and altered wave climate (Saji et al., 1999; Cai et al., 2014; Kumar et al., 2019).

In front of this background, the purpose of this study is to explore the status of and processes behind sediment distribution around the island, their significance for beach formation and coastal erosion, and to elucidate the importance of morphodynamic responses to ocean-borne hazards for low-regret and nature-based climate change adaptation. This study is the first scientific examination on the status and drivers of morphological activity on Fuvahmulah, advancing the design basics for adaptation solutions to sea level rise and wave impacts on small, low-lying coral reef islands. With this, the study also aims to present valuable methods applicable for future studies on other islands:

This study presents high resolution topographic measurements from three field campaigns on the fringing coral reef island of Fuvahmulah. These measurements reveal seasonal shoreline changes and characteristic sediment depot location for the wet and dry seasons in 2017 and 2019. A process-based, empirical

method is combined with multi-directional ocean wave data of hourly resolution from a global reanalysis model (C3S, 2017). The empirical method captures the natural, monsoon-driven seasonal as well as the annual variations of the local hydro- and morphodynamic regime. In addition, numerical modeling efforts help to further analyze coral sediment entrainment, transport processes and distribution on the reef and around the island, dependent on wave directionality and forcing.

These approaches mimic the natural seasonal and annual variations of the typical local hydro- and morphodynamic regime. Considering multi-directional wave input facilitates evaluating characteristic regional and local wave climate as well as following the probable sediment pathway around the island. Compared to studies on annual or seasonal scale, the hourly temporal resolution of hydrodynamic data gives new and more detailed insights into drivers of morphodynamics on reef islands and thus improves the understanding of sediment distribution.

The results of this study facilitate the understanding of sediment transport on reefs and thereby emphasizes the necessity of this natural sediment supply for the island. Previous studies found that the reef serves as temporally varying sediment supplier (Hamylton et al., 2017; Kench and Mann, 2017; Ryan et al., 2019) and the wave climate as sediment distributor on the reef (Kench and Brander, 2006; Kench, 2012; Mandlier and Kench, 2012; Pomeroy et al., 2015, 2017; Shope and Storlazzi, 2019). This study builds on these findings, scrutinizes the influence of a varying wave climate on reef sediment pathways, and thereby showcases reef islands' capability to naturally cope with changing ocean and climate pressures on reef islands. In the face of rising seas, this potential must be considered in coastal management and improves conventional and alternative coastal protection measures for sustainable low-regret coastal adaptation.

2. METHODS

2.1. Study Site

Fuvahmulah is the biggest single reef island in the Maldives that is not part of an atoll and the third largest Maldivian island by population (∼8,510 inhabitants). The low-lying island is located in the Indian Ocean, ∼30 km south of the equator at latitude −0.30° and longitude 73.43° (**Figure 1**). Fuvahmulah is the second most southerly atoll in the Maldives, neighboring Huvadhu Atoll in the north and Addu Atoll in the south. Fuvahmulah is ∼490 km south of the capital Malé. Tide data from the University of Hawai'i sea level Center (UHSLC, Caldwell et al., 2015) shows that the tidal signal on Fuvahmulah is a mixed semidiurnal tide (see **Supplementary Material**) with a maximum tidal range of about 1.1 m. Associated tidal currents (and ocean circulation velocities) are about an order of magnitude below those induced by waves (David et al., 2019).

Fuvahmulah is protected by the fringing reef and a vegetated coastal ridge which surrounds the island. The island's community has a tendency to prefer hard-coastal infrastructure due to national guidelines, but are open toward soft coastal protection measures (Ratter et al., 2019). Today, the island is subject to erosion being introduced by the existing coastal infrastructure (David et al., 2019; Ratter et al., 2019). The seaport is in operation since late 2004, and was constructed with sheltering breakwaters and a port entrance to the north east. But Fuvahmulah also accommodates highly morphodynamic areas: One example is the beach and coastal spit Thoondu in the north. The inhabitants of Fuvahmulah strongly identify with the island in terms of weather-related, seasonally-driven hydrodynamic characteristics, and unique morphodynamic features on Thoondu and the adjacent beaches (Ratter et al., 2019).

Future risks of flooding increase on Fuvahmulah, as on any low-lying islands, because the sea level is projected to rise about 0.8–1.0 m (Magnan et al., in press) and moreover, sea level rise is accelerating in the Indian Ocean (Dangendorf et al., 2019). In the face of climate change, other factors add to the increasing risk by sea level rise: For example, the IOD is a natural oscillation of sea surface temperatures between the western Indian Ocean (50–70° E, 10° N–10°E) and the tropical southeastern Indian Ocean (90–110° E, 10° N–0°), comparable with the El Niño and La Niña oscillations (Saji et al., 1999). Above or below a threshold of ±0.4–0.7°C the dipole has noticeable implications on the climate and weather in the Indian Ocean (Saji et al., 1999; Hermes et al., 2019). The Dipole Mode Index (DMI) is an indicator for the IOD and peaked at a threshold of +2.15 °C in October 2019 (see **Supplementary Material**). A positive DMI leads to an inverse atmospheric convection, and thus winds, from east to west. Extreme, positive IOD events are projected to increase (Collins et al., in press), having an impact on the wave climate and seaborne hazards on small islands in the Indian Ocean (Kumar et al., 2019).

2.2. Wave Data

Measured wave data for the southern Maldives is scarce. Therefore, this study uses publicly available hourly data on single levels from 1979 to November 2019 (C3S, 2017), taken from the ERA5 of the European Centre for Medium-Range Weather Forecasts (ECMWF). Statistical wave data in this paper is given in mean ± standard deviation, if not stated otherwise. The global climate reanalysis model has a spatial resolution of 0.25° in both latitudinal and longitudinal direction. The hydrodynamic boundary conditions for Fuvahmulah in this study come from the node at 0° latitude and 73.5° longitude (**Figure 1**). This data describes the hydrodynamic regime and has a sufficient resolution to be used as boundary condition for regional studies. The significant wave height H_s from the ERA5 data set shows a general trend of wave heights over 1 year (**Figure 2A**) which facilitates classifying the data into wet and dry season. The significant wave height H_s is the average wave height of the 33 % highest waves in a time-series (time-domain) or the integrated energy from a wave spectrum (frequency domain). The directional components are divided in wind-wave and total swell: Here, subsets of a directional wave energy spectrum that are subject to wind forcing are defined as wind-waves. On the contrary, swell subsets are defined as the remaining part of the spectrum that are not wind-waves (Hanson and Phillips, 2001; Bidlot, 2016) and typically subject to larger wave lengths. The ERA5 data set also provides further gradation of swell partitions (with an associated subset of wave parameters), where the swell is divided into the three most energetic systems within the swell

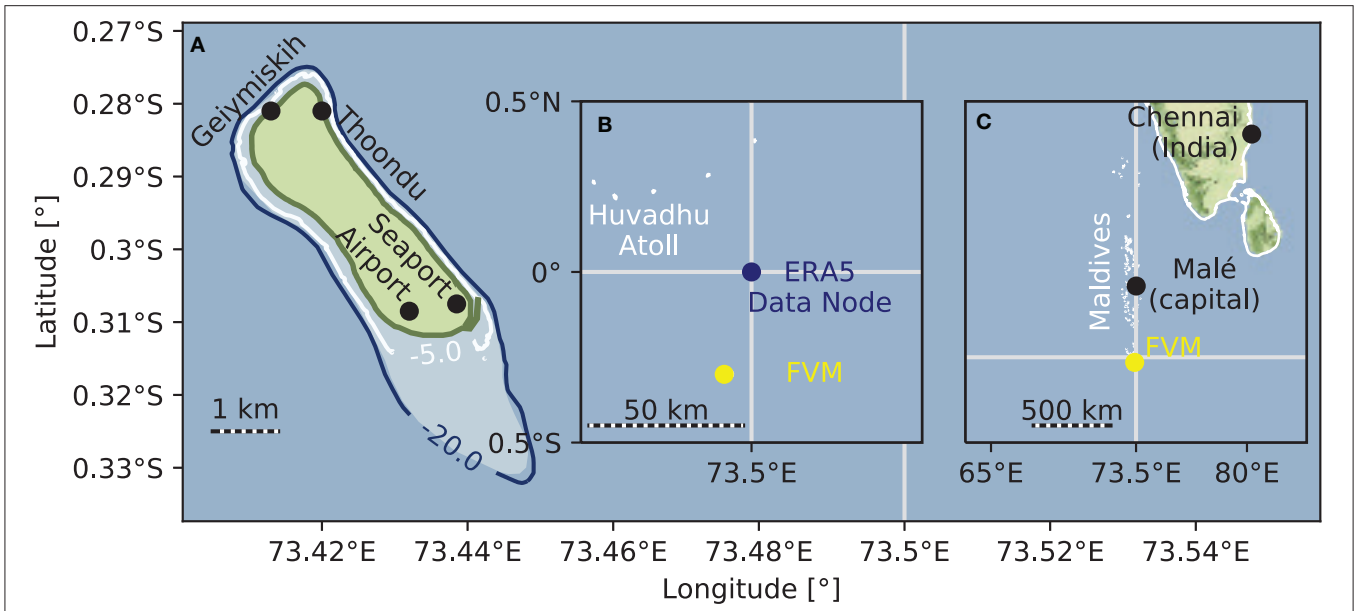

FIGURE 1 | Location of FVM. **(A)** Shows the extent of the island and the fringing reef. It also illustrates the position of the air- and seaport, as well as the beach of Thoondu and the coastal spit. The bathymetry lines come from echo-sound measurements of the first field survey (March 2017). **(B)** Shows the location of Fuvahmulah in the Indian Ocean. The data node is the virtual wave gauge at 0° latitude and 73.5° longitude. In this study, the virtual wave gauge provides information on the wave climate, based on the ERA5 data assimilation of hourly single levels from 1979 to near present (C3S, 2017, see **Figure 2**). **(C)** Shows the island location within the Maldives, Indian Ocean and the location referred to south India and Sri Lanka. Plots were generated with Matplotlib version 3.1.1 (RRID:SCR_008624) and Cartopy. Cartopy also delivered the coastlines in **(B,C)**.

partition (Bidlot, 2016). Each subset and partition contain their own parameters: significant wave height H_s, peak period T_p, mean period T_m, and peak direction θ_p. The mean period is the average time of consecutive waves to pass through a fixed point, while the peak period and direction refer to the wave period and direction associated with the highest spectral energy (C3S, 2017). The division into wind-waves and swell gives an overview of the general wave climate of Fuvahmulah (**Figures 2B–E**). This data is later used to compute and assess sediment transport processes in an approach provided by the Coastal Engineering Research Center (CERC) of the U.S. Army Corps of Engineering (CERC, 1984). The adequacy and flexibility of the CERC formulation has been proven for typical sandy shorelines (Schoonees and Theron, 1995), but application to coral reef transport is rare in literature (Shope and Storlazzi, 2019). Analyzing all peak directions θ_p of each season and wave partition will yield a pre-dominant range or significant range of peak directions $\theta_{p,sig}$. Here, this range is derived from a discrete probability distribution of the whole ERA5 time-series and contains the directions, which combined have the highest 33 % occurrence probability (see **Figure 2** and **Table 1**).

2.3. Field Campaign

Three field campaigns provided data to evaluate the seasonal and annual sedimentation processes around the island: The first campaign started in March 2017 at the end of the dry season. The second field campaign took place at the end of the wet season in September 2017, revealing seasonal variations in combination with the former measurements in March. The last field measures were taken in March and April 2019, disclosing seasonal and annual changes of sediment volumes when compared to the data recorded in 2017. The first field campaign also accommodated a bathymetric survey, recording depth profiles with a dual-frequency echo-sounder (Dr. Fahrentholz LituBox 15/200). Furthermore, the field campaigns yielded the following data sets:

2.4. Digital Elevation Models

The basis of the digital elevation models have been aerial images of the island, recorded by a DJI Phantom 4 (field campaign 1 and 2) and a DJI Phantom 4 Pro (field campaign 3). These unmanned aerial vehicles (UAVs) captured the entire coast of the island, except the beaches directly neighboring the airport. These $\sim$ 1.7 km of the total $\sim$ 11 km long coastline adjacent of the airport lie within a restricted no-fly-zone. The drones captured the accessible coast in 15 tiles, which were used throughout all three campaigns. The drones contain a built-in global navigation satellite system (GNSS) with regular GNSS precision of 2–5 m (Wing et al., 2005). This information serves as first estimation of camera locations in a geodetic reference system for the photogrammetric reconstruction of the beach. Ground control point (GCP) measured with survey grade GNSS devices improve the positioning of the final digital elevation model (DEM) in the geodetic system. Post-processing of the first two campaigns revealed a sub-par precision for the base stations of each tile in World Geodetic System 1984 (WGS84). With the base station's default survey-in time of 15 min, the vertical precision of the position was in the range of 3–7 m vertically, even though the real-time kinematic (RTK) accuracy

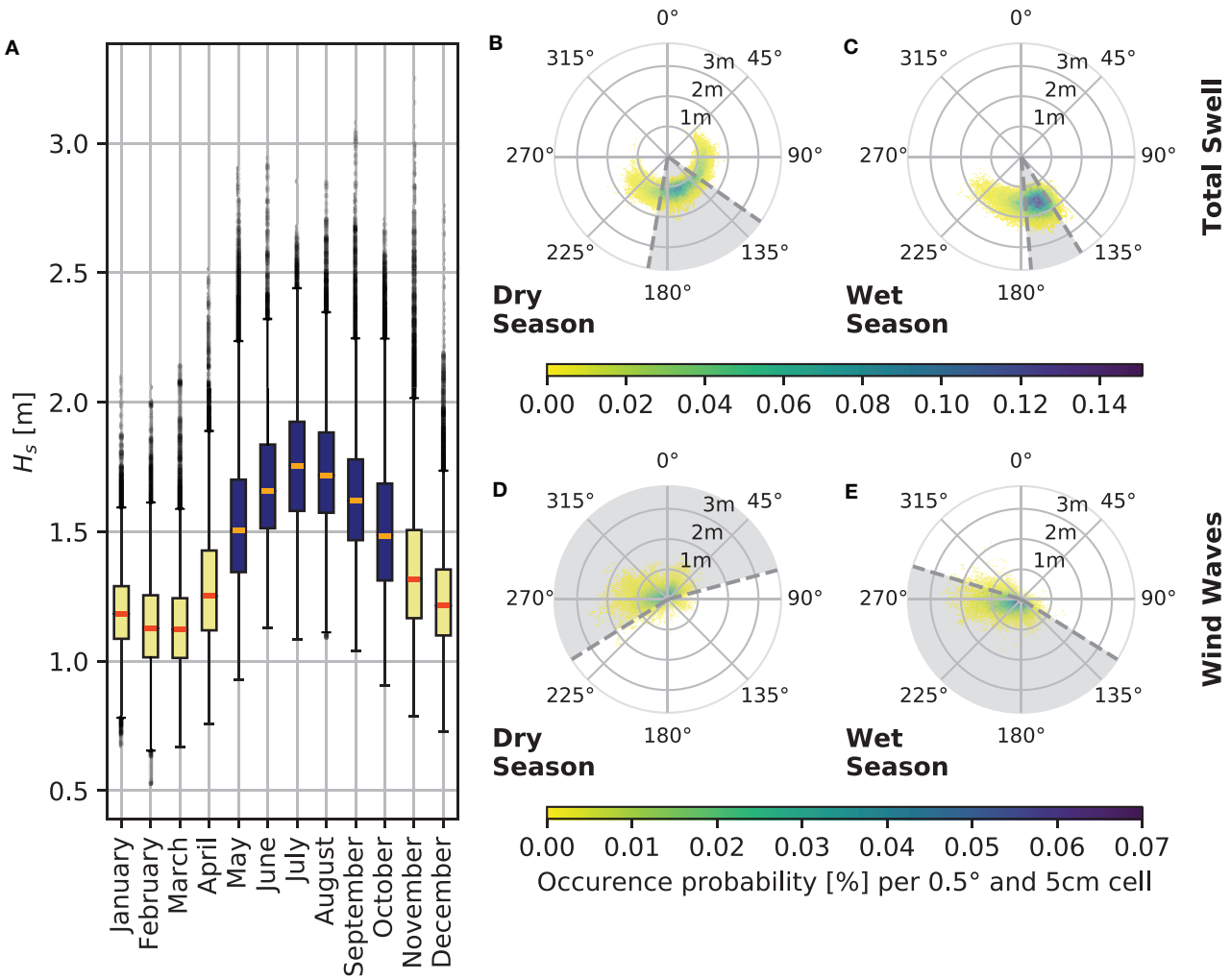

FIGURE 2 | Wave climate at the ERA5 data node (**Figure 1**) **(A)** Shows monthly box plots of hourly significant wave height H_s for a time series from 1979 to 2019. Here, blue boxes are wet season months and yellow boxes are dry season months. **(B)** Shows the discrete marginal distribution between the peak wave direction θ_p and the significant wave height H_s of the dry season, while **(C)** contains this information for the wet season. Both plots use only swell data, while **(D,E)** contain the same information for wind waves. Here, the colorbar shows the occurrence probability of each 0.5° wave direction and 0.05 m wave height cell. The gray areas visualize the significant peak direction range $\theta_{p,sig}$ for each subset, containing the directions which combined have the highest 33% occurrence probability.

of each measured tile remained within centimeter precision (equipment: Trimble 4700 and 5700 receiver, Zephyr and 13″ GPS antennas). To improve the initial positioning, the third campaign included a constant reference measurement combining a Javad Legacy GNSS base station receiver with a NAVX-3G antenna mounted on a roof. The rover consisted of a Septentrio AsteRx-U receiver and another NAVX-3G antenna, recording between 13 and 26 GCP per tile. The GCP measurements were corrected with the signal of the reference point by RTKLIB 2.4.3 b31 (RRID:SCR_018116). The aerial images and the GCPs of the third campaign were then post-processed in Agisoft Photoscan 1.4.5 build 7354 (RRID:SCR_018120) to DEMs of each tile. The DEMs have a resolution of 3.6 cm px^{-1}. Combining both the GNSS deviation and the software estimation by Photoscan, the DEMs have a total median positioning error of $\tilde{\sigma}_{DEM,3} = \pm 6.2$ cm (see **Supplementary Material**). The DEM-tiles of the third campaign then served as reference tiles for the DEMs of the other campaigns: extracting the position of unique features from each tile (for example man-made or reef structures) delivered virtual Ground Control Point (vGCP). These vGCPs were then used to correct the positions of DEMs obtained from the first two campaigns. The median relative error between the DEMs of the dry season 2019 (reference) and 2017 is $\tilde{\sigma}_{vGCP} = \pm 12.7$ cm. Between the DEMs of the dry season 2019 and wet season 2017, the median relative error is $\tilde{\sigma}_{vGCP} = \pm 13.6$ cm. The error of both GCPs and vGCPs is within the usual error range for UAV-borne photogrammetry (Casella et al., 2020).

2.5. Sediment Budgets

In the next processing step, Quantum GIS (version 3.4.11.) uses the rastered topography provided by Photoscan to calculate the

seasonal or annual changes of the coastal topography with

$$\Delta\mathrm{DEM}_{\mathrm{seasonal}} = \mathrm{DEM}_{\mathrm{wet\ season,\ 2017}} - \mathrm{DEM}_{\mathrm{dry\ season,\ 2017}} \quad (1)$$

and

$$\Delta\mathrm{DEM}_{\mathrm{interannual}} = \mathrm{DEM}_{\mathrm{dry\ season,\ 2019}} - \mathrm{DEM}_{\mathrm{dry\ season,\ 2017}} \quad (2)$$

resulting in a difference of topographic height $\Delta z_{i,j}$ for each pixel of the rastered DEM. All further post-processing (**Figure 3**) was performed with the Python module Rasterio (version 1.1.1): The total volume change in each of the ΔDEM is calculated with

$$\Delta V_{\mathrm{DEM}} = \sum_{i=1,j=1}^{i_{max},j_{max}} \Delta z_{i,j} \cdot A_{\mathrm{pixel}} \quad (3)$$

using the area A_{pixel} covered by each pixel in the raster image of each DEM and the associated $\Delta z_{i,j}$ at the pixel's position i and j within the DEM. Because the accuracy of submerged topography tends to be poor (Casella et al., 2016), wet areas were cropped from the DEMs. This results in morphological cells, dividing Fuvahmulah's coastline subsequently into 12.5 m wide sections ranging over the entire dry length of the beach (see **Figure 3B**). The dry beach length does not differ significantly between seasons—except for the northern part of Fuvahmulah. To account for varying beach lengths and to compare the sediment volumes independently of dry beach length, this study assesses the volume change of each morphological cell ΔV_{mc} over it's dry beach area A_{mc} in terms of areal sediment difference Δv_{mc} (**Figure 3**):

$$\Delta v_{\mathrm{mc}} = \frac{\Delta V_{\mathrm{mc}}}{A_{\mathrm{mc}}} \quad (4)$$

here, ΔV_{mc} equals to ΔV_{DEM} but only within the boundaries of the morphological cell (index mc). Summarizing the areal sediment volumes of each morphological cell for the entire island with the absolute areal sediment difference quantifies the morphodynamic activity and gives an estimate on the average shoreline change (index sc):

$$\overline{v}_{\mathrm{sc}} = \frac{1}{m} \cdot \sum_{m=1}^{m} \left| \frac{\Delta V_{\mathrm{mc}}}{A_{\mathrm{mc}}} \right| \quad (5)$$

Another classification of seasonal shoreline change is the island oscillation index I_o (Kench and Brander, 2006). It looks at areas which are subject to $\geq$ 50 % of the maximum shoreline change and relates them to the entire island perimeter. The results give information on the seasonal morphological activity on an island and classify specific characteristics: A high oscillation index implies coastline changes around the entire island between the seasons. Small oscillation indices indicate changes predominantly around a hotspot. Low oscillation indices are typically found on elliptical islands and indicate that large parts of the shoreline are meant to be morphologically stable (Kench and Brander, 2006), if not obstructed by coastal infrastructure (Kench, 2012). This study modifies the approach of Kench and Brander (2006) and uses the average seasonal and annual sediment difference as the volumetric change per area (**Figure 4** and Equation 4) to calculate I_o. Areas that were especially challenging to align and geo-reference in the photogrammetric process, or which were inaccessible due to no-fly-zones, are not taken into account in the sediment budget (**Figure 3**).

Obtaining total sand volumes on beaches with high seasonal differences in beach widths require interpolating the reef height between the base of the wider beach profile and the base of the plain beach (the base of a beach is also called beach toe). The location of the beach toe was derived from orthophotos at low-tide. Interpolation was done for Geiymiskih beach in the north and northwest of Fuvahmulah (**Figure 4**, profile 1). In addition, the Thoondu sand spit forms in the wet season. The wet season associated with higher waves and thus higher run-up, hampering a full reconstruction of the beach face. Therefore, the wet season Thoondu beach is interpolated between the beach crest and the beach toe (**Figure 4**, profile 2). Here, the geodetic height of the reef at the beach base was interpolated from the georeferenced 2019 measurements of the adjacent beach on the east (**Figure 4**, profile 3), where it is at $\sim$ −94.8 m. All interpolations have been done with the interpolation sub-package in SciPy version 1.3.3 (RRID:SCR_008058 under Python version 3.7.3 RRID:SCR_008394). Calculating total sand volumes on dry season beaches at Thoondu leads to further challenges (**Figure 4**, profile 3): On the one hand, large areas of the reef were covered with sand in the dry season, making vGCP assignment on the sea-side of the beach impossible. On the other hand, the land-side is densely vegetated, so that DEMs contain areas with either poor or without referencing. To overcome these challenges, six beach profiles support the estimation of sand volumes on the dry season Thoondu beach. The profiles have been manually referenced to the plain beach in wet season.

Bio-erosion at neighboring islands was assessed as $G_{\mathrm{sed}} = 3.4 \pm 0.4\,\mathrm{kg\,CaCO_3\,m^{-2}\,yr^{-1}}$ (Ryan et al., 2019). This study acknowledges the difference between gross and net carbonate production and bio-erosion (Chave et al., 1972), but in the following, *sediment production* refers to the bio-eroded marine aggregates of the reef, available to be transported toward the island. The corresponding reef area A_{reef} of the Gnaviyani Atoll is 499.2 ha and originates from shape files for the Maldives, provided by ©OpenStreetMap contributors. Combining the annual areal carbonate production rate with the reef platform gives the total annual estimate of sediment volume produced on the reef as

$$Q_{\mathrm{reef}} = \frac{G_{\mathrm{Sed}}}{\rho_{\mathrm{s}}} \cdot A_{\mathrm{reef}} \quad (6)$$

with a measured sediment density of $\rho_{\mathrm{s}} = 2\,\mathrm{g\,cm^{-3}}$.

2.6. Sediment Transport

The CERC-formulation or Shore Protection Manual (SPM)-method for longshore sediment transport (CERC, 1984) uses the longshore component of wave power as longshore wave energy flux

$$P_{y,wp} = c_b \cdot \frac{1}{8} \cdot \rho \cdot g \cdot H_{b,wp}^2 \cdot \frac{1}{2}\sin(2\theta_{b,\perp,wp}) \quad (7)$$

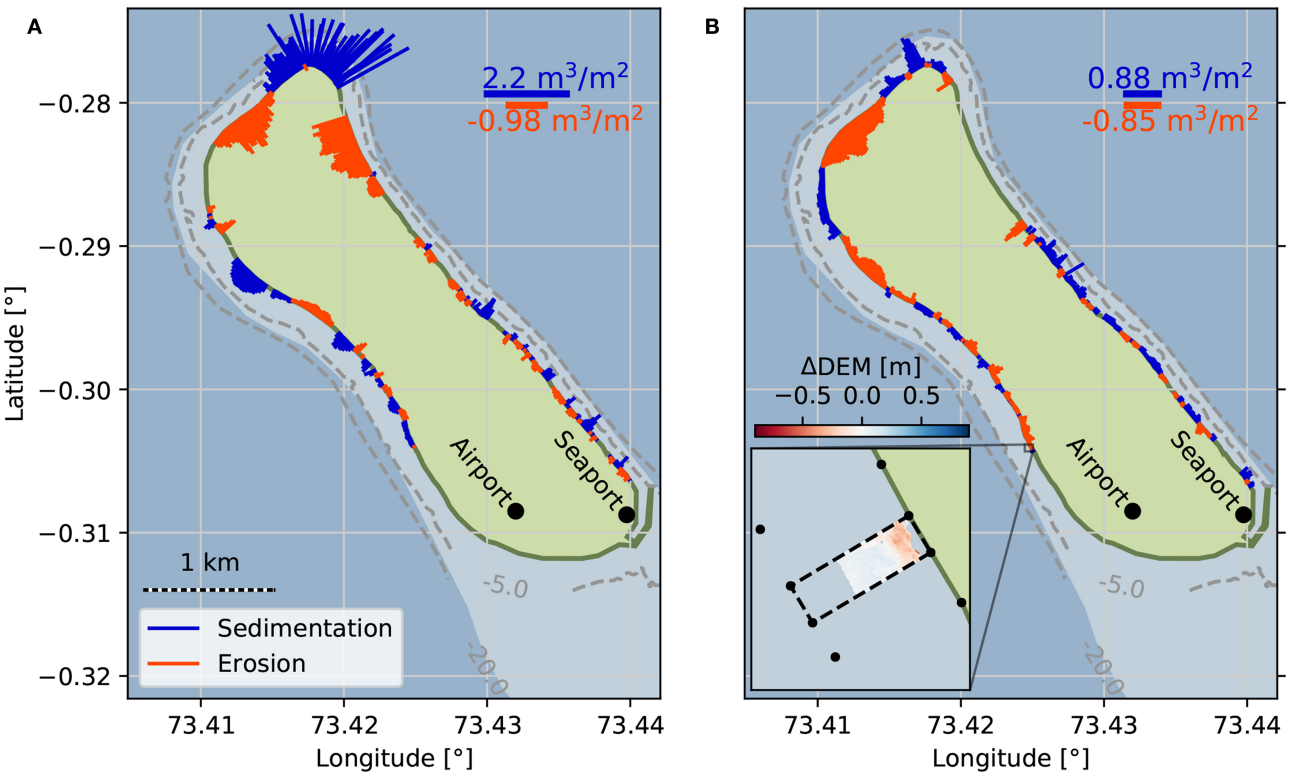

FIGURE 3 | Average areal sediment budgets from DEMs with **(A)** seasonal sediment budget from dry to wet season, based on the data of March 2017 and September 2017 and **(B)** annual sediment budget between dry season 2017 and 2019 (both recorded in March). In both subfigures, sediment accumulation for the observation period is blue, while sediment removal is red. The volumetric change of sediment [m^3] is averaged over dry beach area [m^2] (see Equation 4). Bathymetry lines (gray, dashed) come from measurements in the first field campaign (March 2017).

with c_b as the wave phase velocity, wave height $H_{b,wp}$ and incident wave angle $\theta_{b,\perp,wp}$ for each wave partition wp at the breaker point b, as well as the water density ρ and the gravitation constant $g = 9.81\,\mathrm{m\,s^{-1}}$. The shear stress of the wave-averaged transport momentum S_{xy} is the longshore transport component when considering $\theta_{b,\perp}$ with respect to beach orientation. The longshore transport component S_{xy} does not vary outside the breaker zone, so that $P = S_{xy,b} \cdot c_b = S_{xy,0} \cdot c_b$, with index 0 for deep water waves (Longuet-Higgins, 1970; Bosboom and Stive, 2015). Converting Equation (7) to deep water parameters with $n_0 = 1/2$ yields:

$$P_{y,wp} = \frac{c_b}{16} \cdot \rho \cdot g \cdot H_{0,wp}^2 \cdot \sin(2\theta_{0,\perp,wp}) \cdot n_0 \tag{8}$$

From linear wave theory, the wave velocity at the breaking point is $c_b = c_0 \cdot \tanh(k \cdot h_b)$ using the water depth of breaking waves h_b and ERA5 wave periods to calculate c_0. The echo-sounder usually recorded depths of around $h_b \approx 4.5\,\mathrm{m}$ where the boat was able to measure close to the breaker line. Further input values for incident waves are the significant wave height $H_{s,wp}$ for $H_{0,wp}$ and peak wave directions $\theta_{p,wp}$ from the ERA5 data set for each wave partition wp. With respect to the coastline normal, the incident angle from θ_p is $\theta_{0,\perp} = \theta_p - \alpha_\perp$, where the coastline normal is $\alpha_\perp$. The incident wave direction $\theta_{0,\perp}$ ranges from -90 to $90°$ with regard of the coastline normal. Values beyond this range are not considered in Equation (8). On the other hand, with $\sin(2 \cdot \theta_{0,\perp})$, oblique waves approaching the coastline normal from $\alpha_\perp = \pm 45°$ will have the greatest impact on longshore sediment transport, while waves from $\alpha_\perp = \pm 90°$ or $\alpha_\perp = 0$ will have no influence on it. The CERC-equation assumes the wave energy flux P_y being the forcing parameter behind changing beach morphology. When considering the local wave angle $\theta_{0,\perp}$ in Equation (8), the wave energy flux P_y already gives information on the expected morphodynamic response of the beach (Rutten et al., 2017). But the CERC-formulation combines the longshore energy flux (Equation 8) with sediment parameters as the *"immersed weight of sand moved"* (CERC, 1984) to translate it into volumetric sediment transport rates:

$$I_{y,wp} = \frac{K}{\rho \cdot g \cdot (\rho_s - \rho_w) \cdot (1 - \Phi)} \tag{9}$$

here with salt water density ρ_w of $1.03\,\mathrm{g\,cm^{-3}}$, sediment density ρ_s of $2\,\mathrm{g\,cm^{-3}}$, a porosity Φ of 0.2, and an empirical coefficient K. Combined, the CERC formulation reads:

$$q_{y,wp} = P_{y,wp} \cdot I_{y,wp} = \frac{K \cdot c_b}{32 \cdot (\rho_s - \rho_w) \cdot (1 - \Phi)} \cdot H_{0,wp}^2 \cdot \sin(2\theta_{0,\perp,wp}) \tag{10}$$

The empirical coefficient K is the transmission between wave-induced energy flux and sediment parameters. It accounts for the heterogeneity of beach sediments and the local coastal environments. The coefficient translates the wave energy impact on site into the site-specific sediment motion by calibration with measured data (Schoonees and Theron, 1995). In this study, K facilitates matching the measured with the calculated total sediment volume of the field campaigns in 2019. Using the CERC-formulation, the total sediment volume transported on a coast for all wave partitions is

$$Q_y = \sum_{wp=wp_{ww}}^{wp_{S3}} q_{y,wp} \tag{11}$$

with wp_{ww} for wind waves and wp_{Si} for swell waves with i for each of the three swell partitions of the ERA5 data set. With the sediment volumes measured in the 2019 dry season field campaign for the northwest (NW: 14.689 m^3) and east coast (E: 1.171 m^3), the empirical coefficient K becomes $K_{NW} = 55.89$ and $K_E = 107.26$.

When illustrating results from the CERC method based on the hourly ERA5 data between January 2016 and November 2019, this study smooths the data with a combined windowed forward and backward average filter based on

$$\overline{H_s} = \frac{1}{2}\left(\frac{1}{n}\sum_{i=0}^{n-1} H_{s-i} + \frac{1}{n}\sum_{i=0}^{n+1} H_{s+i}\right) \tag{12}$$

with a window of $n = 24\,\mathrm{h} \cdot 7\,\mathrm{d}$. Filtering was applied on H_s (depicted in Equation 12), θ_p, q_y, and Q_y (analogous to Equation 12). Smoothing accounts for a delayed response of the morphology to wave energy forcing (Rutten et al., 2017).

2.7. Modeling

This study also uses the wave data from ECMWF's global reanalysis model ERA5 as boundary condition in the phase-resolving, depth-integrated Boussinesq Ocean and Surf Zone model (BOSZ). The governing equations of BOSZ fall into the category of Boussinesq-type equations—an approximation of the Navier-Stokes equations commonly used for studies of coastal areas (Roeber et al., 2010; Roeber and Cheung, 2012). These governing equations compute dispersion accurately for water depths up to $kh \approx \pi$, with k as wave number and h the water depth (David et al., 2017). For deep waters of $kh > \pi (k = 2\pi/L)$ BOSZ starts overestimating the wavelength (L) increasingly. Previously, the numerical model has been used for example in modeling cascades to compute wave transformation and associated impacts over irregular bathymetries, such as reefs (Roeber and Bricker, 2015) and to study shorter, more non-linear wave phenomena (David et al., 2017). BOSZ uses an adaptive wetting and drying algorithm and has shown good results when benchmarked with laboratory and field data of different scenarios (Horrillo et al., 2014; Lynett et al., 2017).

In this study, the model uses the off-shore ERA5 wave data to compute wave propagation and transformation from deeper to shallow waters, leading to wave-induced currents on the reef surrounding Fuvahmulah. The reef's bathymetry originates from echo-sounder measurements recording data until a maximum depth of about 45 m. The minimum water depth from the echo-sounder depends on the required under keel clearance of the boat, being at water depths of about 4 m. As complement to the bathymetry, the DEMs (wet season, 2017) supply topographic information on the coastal and intertidal areas of the reef. The reef topography's elevation data starts approximately at around mean low tide. The Generic Mapping Tool (GMT) combines the bathymetric and topographic data, projecting it onto a computation grid with 876 × 1,274 cells and a $\Delta x, \Delta y = 7.5$ m resolution (Wessel and Luis, 2017). Off shore waters are limited to 60 m depth to maintain an effective dispersion accuracy for the governing Boussinesq-type equations. The model contains a hydrodynamic framework, providing for example water level elevation and wave-induced currents on the reef in form of depth-averaged flow velocities (for a snapshot of the free surface elevation provided by BOSZ see **Supplementary Material**). The resulting, two-dimensional velocity fields are the main drivers behind sediment transport on the beach (van Rijn, 2005), revealing areas of sediment pick-up at increased, and accretion areas at reduced velocity gradients. On Fuvahmulah, ocean circulation and tidal currents are significantly lower than those of wave-induced currents (David et al., 2019) and, in general, are of minor importance when modeling longshore sediment transport (Burcharth et al., 2007). Therefore, this study accounts for currents induced by waves from the dominant wave direction $\theta_p = 157.5 \pm 22.5°$, in a TMA-spectrum with a significant wave height $H_s = 2.3$ m, and peak period of $T_p = 17$ s over a bathymetry with constant Manning's friction of $n = 0.013\,\mathrm{s\,m^{1/3}}$. The friction parameter was chosen in accordance to another study with the same model over coral reefs (Roeber and Bricker, 2015).

3. RESULTS

3.1. Wave Climate and Tidal Regime

Fuvahmulah has two seasons: the wet or rainy season from May to October and the dry season from November to April. Between the wet and the dry season, waves differ in height as shown by the ERA5 data set (C3S, 2017) of the ECMWF (**Figure 2**). While the dry season brings northeastern winds, Fuvahmulah is subject to mainly south to southwestern Monsoons in the wet season (MEE, 2014). The Monsoons are accompanied by high waves with the highest median significant wave height in July ($\tilde{H}_{s,\mathrm{max.}} = 1.72$ m), while the highest total significant wave height was registered on November, 5th 2016 ($H_{s,\mathrm{max.}} = 3.25$ m). While this study defines November already as dry season, the wave data discloses a transition phase between wet and dry season. The lowest annual median value $\tilde{H}_{s,\mathrm{min.}} = 1.12$ m appears in March (dry season).

Observations of the wave climate during the field campaign have shown that waves approach the island from multiple directions at the same time. This is important for the further analysis and significant for the coast as well as coastal structures, because it reveals the need for multi-directional data. To analyze the multi-directional wave climate, the ERA5 data set provides hourly wave parameters, such as significant wave height H_s and

TABLE 1 | Wave parameters for the time series at the ERA5 data node (**Figure 1**).

	Dry season		Wet season	
	$\overline{H}_s$	$\theta_{p,sig}$	$\overline{H}_s$	$\theta_{p,sig}$
Swell waves	1.17 ± 0.18 m	125–190° (SE-E)	1.60 ± 0.26 m	148–175° (SE-E)
Wind waves	0.26 ± 0.28 m	238–75° (SW-E)	0.26 ± 0.28 m	122–287° (SE-W)

*The table contains the mean significant wave heights H_s as well as significant peak direction ranges $\theta_{p,sig}$ (**Figure 2**) for wind waves and swell approaching Fuvahmulah.*

peak wave direction θ_p for both wind waves and swell partitions for ocean waves from 1979 to 2019 (C3S, 2017). These parameters are used to describe the dominant features of wave heights, periods and directions:

Around Fuvahmulah, total swell has a higher seasonal variation of H_s but less spreading or directional variety of associated peak wave directions θ_p than wind waves (**Figure 2** and **Table 1**) Swell waves are rarely below 1 m in the wet season (**Figure 2**. The dominant peak direction $\theta_{p,ts}$ are coming from south to southwest in both seasons, however the dry season contains additional directional components between ∼45 and 135°, which are absent in the wet season.

Wind waves have a mean significant height of $\overline{H}_{s,\mathrm{ww}} = 0.26 \pm 0.28$ m (in both seasons, **Figure 2** and **Table 1**). The highest wind waves approach the island from west. The two significant differences among seasonal wind waves are (a) in the dry season waves reach Fuvahmulah dominantly between 238 and 75° while they approach the island with 122–287° in the wet season and (b) an additional north to west (0–90°) component in the dry season being absent in the wet season. Both differences have a considerable influence on the sediment transport in the northern part of the island and the sand spit Thoondu.

Summing up the above, the wave climate around Fuvahmulah is characterized by dominant southerly swells with noticeably higher waves in the wet season than in the dry season. The main swell direction $\theta_p \sim 157.5 \pm 22.5°$ is similar to the orientation of the large southeastern reef. Both seasons occasionally experience (wind) waves from west, however the dry season has a much higher angular spreading for both wave components. The dry season has an additional swell component from northeast to southeast and a wind-wave component coming from northern to eastern directions. These components are absent in the wet season. Analyzing the hindcast wave data reveals the difference between seasons: Monthly time series of wave heights from 1979 to 2019 show a gradual transition between wet and dry seasons without a fixed date explicitly terminating a season (**Figure 2**). Dominant south to southeastern swells and increased wave heights in the wet season define the characteristic hydrodynamic regime for the Maldives (Kench and Brander, 2006; Kench and Mann, 2017).

3.2. Sediment Budget From Measurements

The Gnaviyani Atoll has a size of 992.3 ha and consists of the island Fuvahmulah, covering an area of 493.1 ha, and the fringing reef with 499.2 ha. The coral reef is the natural sediment source for the island with an estimated annual sediment production rate of $3.4 \pm 0.4\,\mathrm{kg\,CaCO_3\,m^{-2}\,yr^{-1}}$ (Ryan et al., 2019), leading to a total sediment supply by the reef of $Q_{\mathrm{reef}} = 8,486 \pm 998\,\mathrm{m^3\,yr^{-1}}$. The total carbonate production rate of the reef depends on the eco-geomorphological zones on the reef platform. These zones are subject to different light availability, wave energy and degree of turbidity. Carbonate production is also affected by anthropogenic, natural and climate stressors that change the water quality and temperature (Hamylton et al., 2017; Ryan et al., 2019). The Gnaviyani Atoll reef is mostly sub-tidal with an inter-tidal reef-flat around Fuvahmulah. The sub-tidal reef fringes the inter-tidal plateau before it expands to an about ∼ 2.2 km long and 1.6–0.5 km wide fore reef in the south east. This southern fore reef makes about 58.8 % of the total reef area. At the southeastern tip of the fore reef, the depth is ∼ 25 m and slowly decreases to around 8–15 m until reaching the inter-tidal reef. The reef form is elliptical with the long axis approximate to the dominant swell wave direction $\theta_p \sim 157.5°$. The transition from sub-tidal fore reef to intertidal reef on the south and west side is sudden, while it is more gradual on the north and east side of Fuvahmulah. The inter-tidal reef is wider on the south and west side (around 85–145 m) than on the north and east side (around 15–25 m).

The sandy western beaches have mildly sloping equilibrium beach profiles, while the eastern beach profiles change from south to north: Long parts of the southern east coast suffer from noticeable erosion introduced after the port construction at the southeastern end of Fuvahmulah (David et al., 2019). The northern part of the east side (Thoondu) as well as the north coast is part of a highly morphodynamically active region (**Figure 3**). This region hosts coarse calcareous sediment to fine pebble stones. The beaches west and south of the airport (in the south and southwest of the island) consists of steep pebble stone beach profiles, which become sandy in front of the port breakwater (south). This sandy accumulation on the sea side of the western port breakwater and in front of the airport runway is blocked by the port infrastructure (Naeem, 2006; David et al., 2019).

3.2.1. Morphodynamic Activity and Seasonal Formation of the Thoondu Spit From Field Data

The island oscillation index I_o describes the morphodynamic activity of an entire island by comparing the island's perimeter with the coastal area encompassing more than half of the maximum (seasonal) coastline change. The coastline change is linked to the beaches' volumetric changes and—in this study—estimated by integrating seasonal and interannual sediment differences over 12.5 m wide areal increments of Fuvahmulah's coast. The underlying sediment differences required for this procedure originate from the DEMs of the UAV surveys.

Averaging these seasonal and interannual mean shoreline changes discloses a higher seasonal than interannual morphodynamic activity. This results from the seasonal mean shoreline change between the 2017 dry and wet season ($\overline{v}_{\mathrm{sc}} = 0.33\,\mathrm{m^3/m^2}$), being greater than the interannual mean shoreline changes between 2017 and 2019 ($\overline{v}_{\mathrm{sc}} = 0.15\,\mathrm{m^3/m^2}$). But shoreline changes in most coastal areas are below these mean

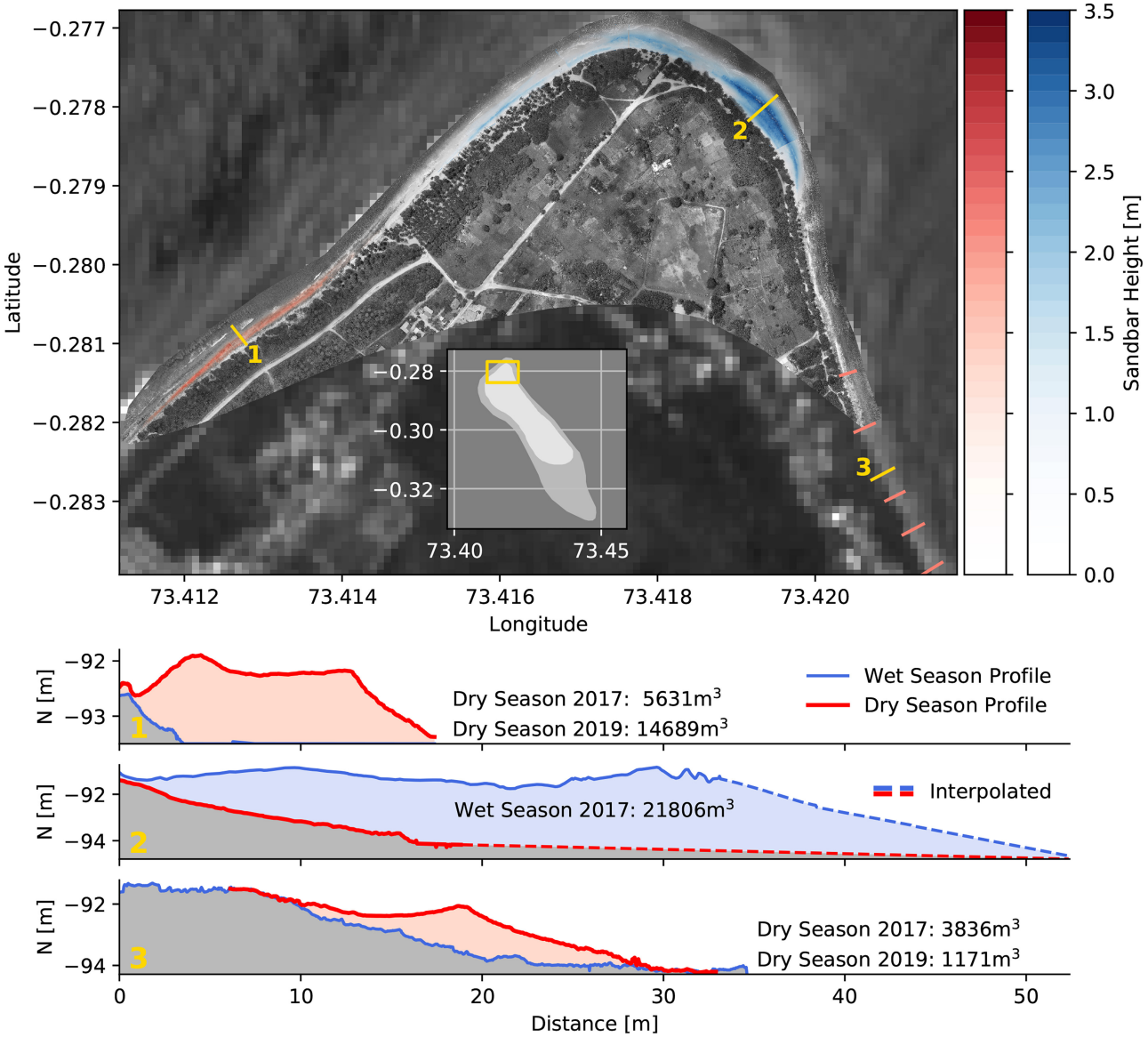

FIGURE 4 | Location of sediment volumes and profiles (orange lines) for the dry season 2017 (red colorbar) and wet season 2017 (blue colorbar) in the north of Fuvahmulah. In the dry season sand depots form at the adjacent beaches Geiymiskih Fannu in the west (profile 1) and Thoondu in the east (profile 3) of the headland. The wet season allocates sand on the north tip of the island, forming the Thoondu sand pit (profile 2). The dry season sand volume of eastern Thoondu beach (profile 3) was integrated over differences of six accuracy-improved profiles. The profile elevation *N* is given as distance to the WGS84 ellipsoid. The background satellite image contains Copernicus Sentinel data (true color, red green blue) from September 14, 2017, which is in the wet season.

values—except for the northern headland. The northern headland is Fuvahmulah's prominent morphodynamic area, but covers only a small fraction of the island's perimeter (**Figure 3**).

Using this information for the island oscillation index leads to a low I_o of $I_o = 350° - 315°/360° = 9.7\,\%$. Such low oscillation indices on elliptical islands indicate that the elongated, lateral shorelines are meant to be morphologically stable (Kench and Brander, 2006) if not obstructed by artificial interference (Kench, 2012), for example harbors, jetties or breakwaters.

Focusing on the prominent morphodynamic area in the north of Fuvahmulah discloses the seasonal formation of the Thoondu spit:

When describing the sheer amount of sediment allocation and (re-)distribution on the northern beaches from experiences and by visual inspection, beaches with a low-lying rocky bottom material in one season can be covered by meter high bulk sediment in the other season. The associated UAV measurements and DEMs reveal two distinct depots in the dry season 2017: The depot on the west side of the headland has a net volume of 5.631 m^3 and is called Geiymiskih Fannu (red area on the

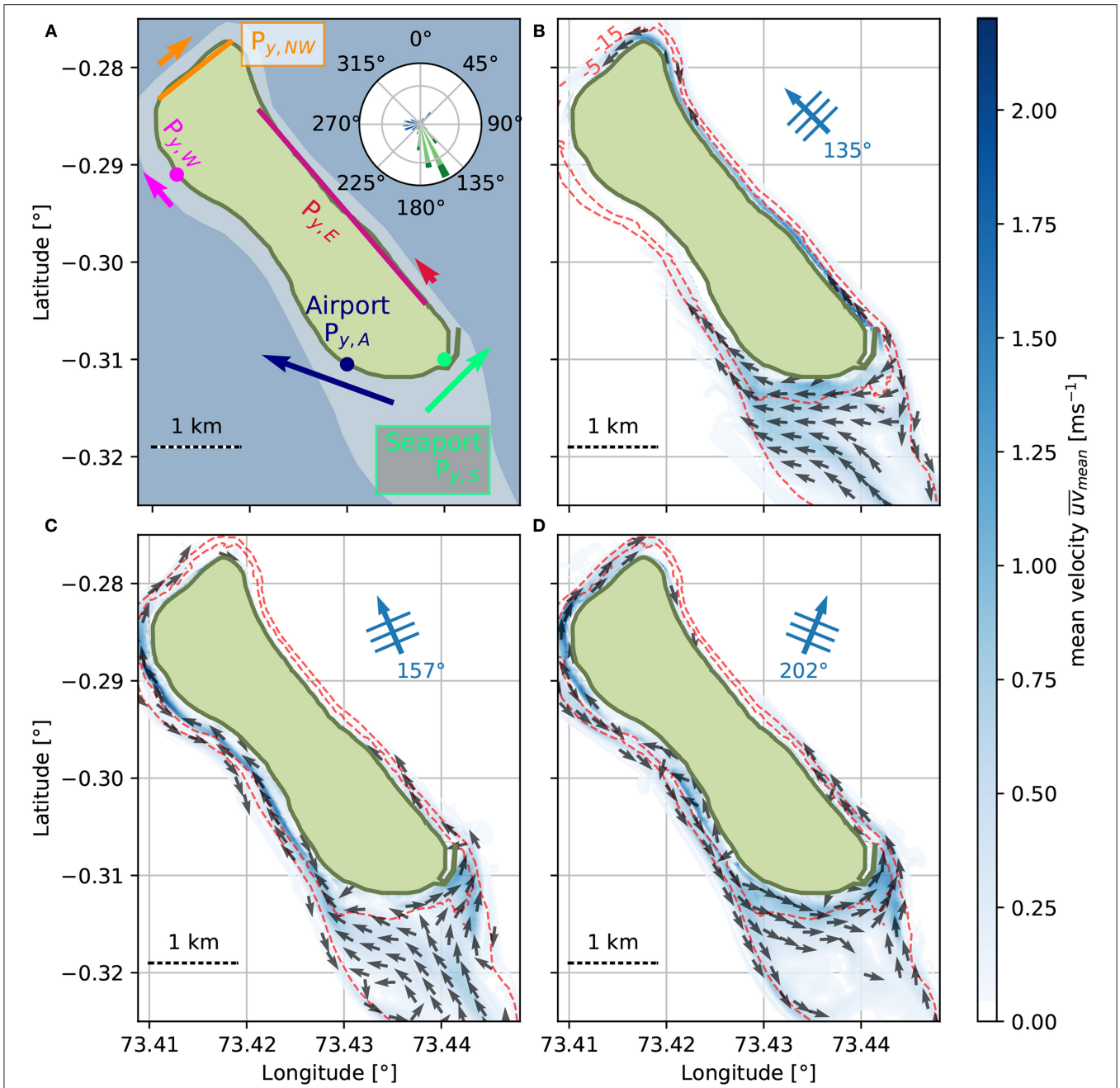

FIGURE 5 | (A) Longshore energy flux rates P_y between 2016 to 2019 indicating sediment transport direction and potential in the CERC-formulation for incoming waves between 2016 and 2019. The wave rose separates annual wind waves (blue) from swell (green). The resulting sediment transport direction is shown in front of the air- and seaport as well as for the beaches on the north and east side. The arrow lengths are in proportion to P_y calculated at each location (values in **Table 2**). **(B)** Current velocities from the depth-averaged, phase resolving numerical wave model (BOSZ) for waves approaching the island from $\theta_p = 135°$, **(C)** $\theta_p = 157.5°$ and **(D)** $\theta_p = 202°$. The background color shows the magnitude of wave induced current velocity on the reef while the arrows depict the local current direction. Dashed red contour lines are the reef depths −5 and −15 m recorded in the first field campaign (March 2017).

map and cross section 1 in **Figure 4**). The depot on the east or southeast side of the headland has a volume of 3.868 m^3 and is part of Thoondu beach (red transects on the map and cross section 3 in **Figure 4**). In total, this makes a volume of 9.499 m^3 for the dry season 2017. Later in the wet season 2017, a large sediment depot with 21.806 m^3 net volume gradually forms on the northern tip of the headland—the Thoondu spit (blue area on the map and cross section 2 in **Figure 4**). The UAV-borne data of the two field campaigns in 2017 discloses a positive seasonal sediment balance. The instantaneous records do not contain the

TABLE 2 | Beach orientation as well as longshore sediment transport directions and energy flux rates P_y, i from the CERC-formulation (**Figures 5A**, **7**, **8**).

Index *i*	Coastline parallel (°)	Longshore transport direction (°)	Mean longshore energy flux $P_{y,i}$ ($\times 10^3$) (kW m^{-1} yr^{-1})
NW	231.6	+180	4.9
E	319.3	+0	0.9
S (Seaport)	45.0	+180	14.6
A (Airport)	110.0	+0	22.3
W	139.3	+180	7.4

The longshore transport directions are expressed with respect to the coastline parallel $\alpha_\perp$.

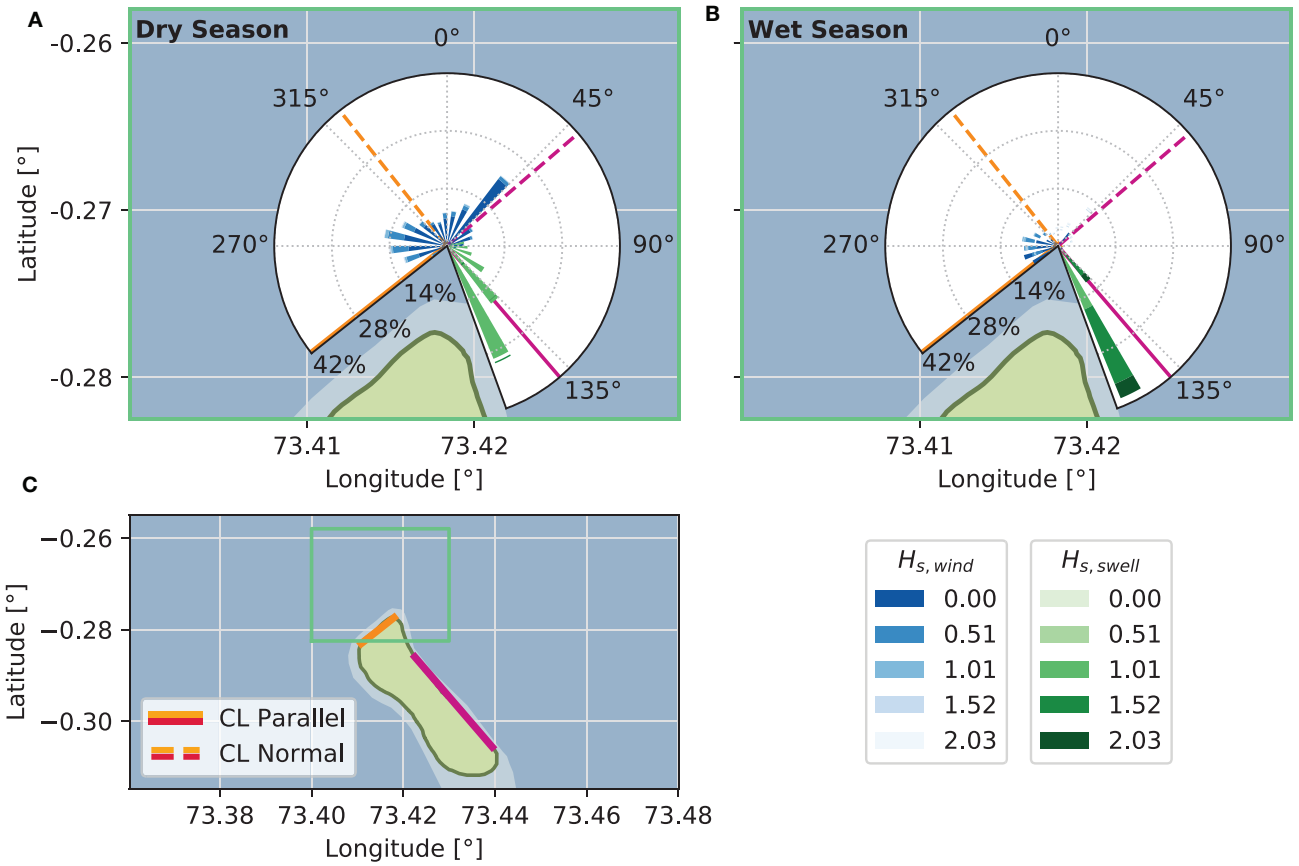

FIGURE 6 | Wave parameter input for the assessment of the evolution of the Thoondu sand spit with the CERC method for **(A)** the dry season and **(B)** the wet season. Blue and green bar plots are the wave rose for wind and swell waves. Orange and crimson lines in the wave roses mark the shoreline parallels (solid) and shoreline normals (dashed) of **(C)** the beaches Geiymiskih (orange, see also **Figure 7**) and Thoondu (crimson, see also **Figure 8**) adjacent to the northern headland.

maximum depot sizes, as the seasonal difference in sediment volume is +12.307 m^3. In the field campaign during the dry season of 2019, sediment depots formed at the same locations as in the dry season 2017. However, the depot in the west (Geiymiskih Fannu) was considerably larger when compared to 2017 (14.689 m^3), while the eastern depot was smaller (1.171 m^3, southeast Thoondu). In total, the sediment volume recorded in the dry season of 2019 is 15.860 m^3. This is an additional sediment volume of +6.361 m^3 over the dry season of 2017, while it is −5.946 m^3 less than in the wet season of 2017.

3.3. Sediment Transport From Models

In this study, two approaches help to study sediment distribution on the Gnaviyani Atoll (**Figure 5**): an empirical, process-based method—the CERC-equation—assesses the longshore transport processes, while the BOSZ model is a numerical approach to compute current pattern on the reef. For the coastlines around Fuvahmulah, the CERC-formulation (CERC, 1984) quantifies the expected longshore sediment transport rate q_y, wp as volume over time for each wave partition wp separately and also the total sediment volume Q_y transported between January 2016

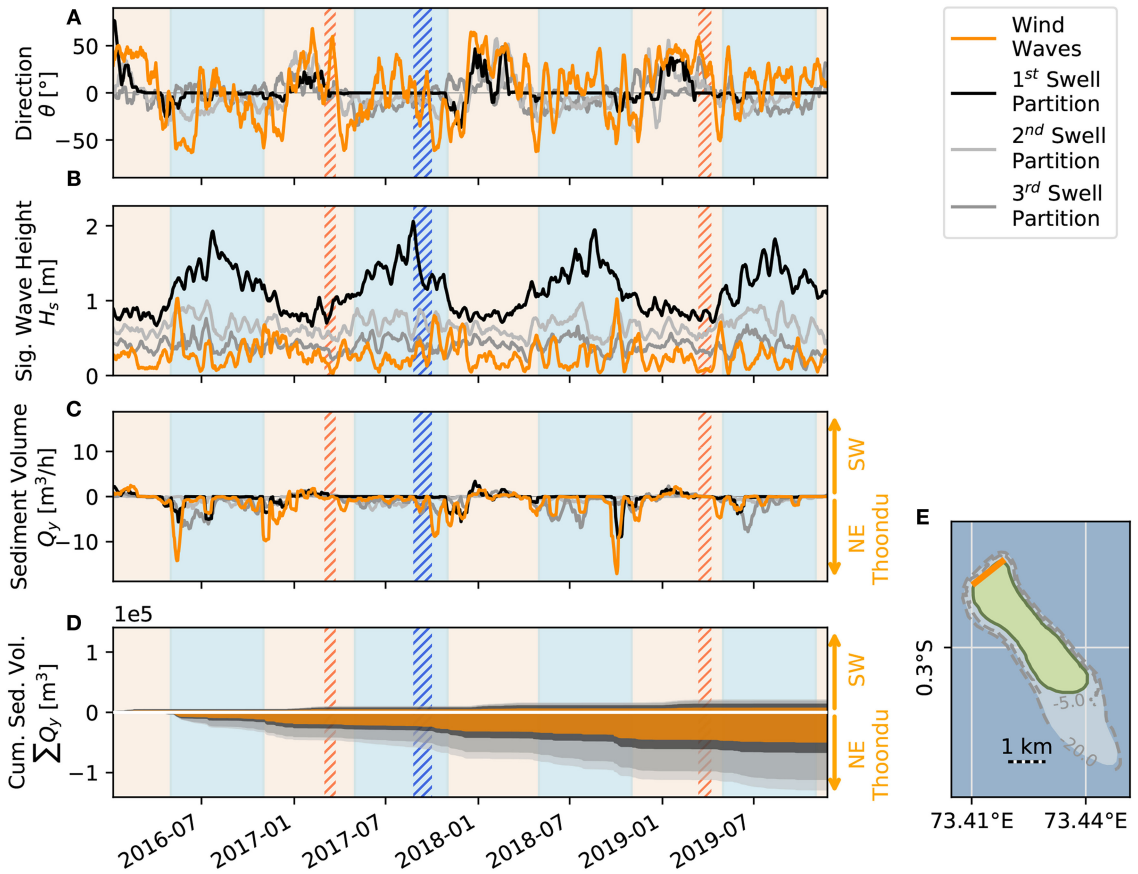

FIGURE 7 | (A) Averaged incident wave direction $\theta_{\perp,wp}$, measured as difference from the coastline normal $\alpha_{\perp}$ and **(B)** wave height $H_{s,wp}$ of each wave partition *wp* used for **(C)** longshore sediment transport rates $q_{y,wp}$ and **(D)** cumulative sediment volume $Q_{y,wp}$, transported alongshore the, marked with an orange line on the map in **(E)**. The orange line is accordance with the orange line in **Figure 6** (see **Table 3** for corresponding peak transport rate values $q_{y,max}$ and the contribution of each wave partition to Q_y). The time series shows values from January 2016 to November 2019. Positive values for $q_{y,wp}$ and $Q_{y,wp}$ indicate a transport toward southwest, while negative values lead to sediment transport toward Thoondu beach in the northeast. The time series shows the dry season with orange and the wet season with blue background. Field campaign 1 and 3 (orange hatched area) took place in March 2017 and 2019. Field campaign 2 (blue hatched area) was conducted in September 2017.

and December 2019. The numerical model depicts wave-induced currents for the dominant swell wave direction $\theta_p \sim 157°$ as well as the outer limits of the dominant swell range with 135 and 202°. The model resolves the wave interaction with the reef spatially (**Figure 2** and **Table 1**). In combination, the empirical and numerical methods can capture the spatio-temporal sediment transport over the reef.

3.3.1. Results From the Empirical Model

Considering the reef crest and reef flat as *carbonate factory for sediment supply to reef islands* (Ryan et al., 2019), the numerical model demonstrates that wave-induced currents transport sediment from the reef toward Fuvahmulah (**Figures 5B–D**). The CERC-formulation assesses longshore energy flux as driver for sediment transport rates around the island on five locations: the southern sea- and airport areas as well as the beaches on the west, northwest and east (**Figure 5A** and **Table 2**). Sediment transport splits on the southern beach into an eastern component at the seaport and a western component at the airport. The lateral beaches have a northward directed transport direction, where the CERC-equation estimates a 6.9 times larger energy transport potential on the west side when compared to the east side. Based on longshore energy fluxes, the longshore transport pattern from the CERC-formulation discloses sediment reaching the island from the southeastern reef plateau will primarily be distributed over the west side. According to the CERC-equation, sediment transport over the east side up to the northeastern headland is of minor significance. The numerical model confirms the general distribution pattern revealed by the CERC-formulation for the dominant swell components (**Figures 5B–D**). It shows that the currents flow around the southern coast and toward the north, where the Thoondu spit forms in the wet season (**Figure 4**) and hints at higher current velocities on the west side from the dominant swell wave direction $\theta_p \sim 157.5°$ (**Figure 5C**).

The beaches of the northern headland are the island's lee side. This area is sheltered against the dominant southern swells and only experiences swell impact through diffraction

and refraction occasionally—the numerical model shows the influence of dominant southern or southeastern swells, leading to currents on the northern beaches Geiymiskih Fannu and Thoondu (**Figures 5B–D**). Suspended sediment entrained in currents is swept along and transported along the west coast toward the north. There, it deposits in areas with mitigated current velocities, as seen in the dry season (**Figure 4**). While being sheltered from the dominant swell waves, data from the wave rose shows that the north coasts of Fuvahmulah dominantly experience wind waves (**Figure 6**). Wind wave induced currents lead to further sediment transport, as shown by the CERC-formulation. The CERC-equation gives further insights in the temporal scale of sediment transport on the northern beaches and facilitates assessing the intraannual evolution of the Thoondu spit (**Figure 4**). It only utilizes waves approaching the coastline normal at $\theta_{\perp} \pm 90°$, excluding swell waves approaching the island from the south (**Figure 6**):

The coastline parallel of the north coast (Geiymiskih beach) is at 231.6°, while the coastline normal is at 319.3° (**Figure 6**, **Table 2**). The combination of wave angle and height defines the amount of sediment longshore transport, peaking at $\theta_{\perp} \pm 45°$ with $\sin(2 \cdot \theta)$ in equation 10. Therefore, longshore transport rates commonly peak at the end of the wet season, with high waves and incident angles of $\theta_{\perp} \sim -50°$ (**Figure 7**). Even though swell waves are dominant around Fuvahmulah, in the CERC-formulation the main share of total longshore sediment transport comes from wind waves (36.8 %) and the second swell partition (33.8 %, **Table 3**). They appear in the wet season or in the transition between dry and wet season. Regarding the CERC-equation's longshore transport direction, only 13.6 % of the sediment longshore rate is toward the south west, while 86.4 % is toward Thoondu beach in the north east. Occasional, single events yield the highest longshore sediment transport rates on Geiymiskih beach (**Figure 7C**).

The coastline parallel of the eastern beach feeding the Thoondu spit is at 319.3°, while the coastline normal is at 49.3° (**Figure 6**, **Table 2**). Significant wave heights are from the same data base as those used at the adjacent Geiymiskih beach (**Figure 7**). Thoondu and the east side of Fuvahmulah are subject to swell waves from the south east, as well as wind waves from north west to north east (**Figures 6**, **8**)—but in contrast to Geiymiskih beach, wind waves have a small overall contribution to the total sediment transport when calculated with the CERC-equation for the east side (17.7 %). Nevertheless, Thoondu beach is prone to receive some of the dominant southeastern swell waves with $\theta_p = 135° - 180°$. However, with respect to the coastline parallel, dominant swell waves approach the beach only with $\theta_{\perp} \leq 9°$, resulting in a low contribution in the CERC-formulation. Instead, occasional first partition swell wave events trigger longshore sediment transport in the CERC-equation, followed by second partition swell waves (**Figure 8** and **Table 3**). The resulting dominant longshore sediment transport direction is toward Thoondu beach (67.9 %). The dominant sediment transport toward Thoondu is commonly found in the course of the wet season, usually peaking between July and early September. Southward components only appear in dry season.

TABLE 3 | Peak transport rates $q_{y,max}$ and the contribution of each wave partition to the total transported sediment volume Q_y in the CERC-formulation between 2016 and 2019 on the northern beaches Geiymiskih and Thoondu (NW: **Figure 7** and E: **Figure 8**).

Beach index *i*	Wave partition index *wp*	Peak sediment transport rate $q_{y,i,max.}$ ($m^3\ h^{-1}$)	Contribution to total transport volume Q_y (%)
NW	Wind waves	17.08	36.8
	1st swell partition	9.31	16.1
	2nd swell partition	7.79	33.8
	3rd swell partition	3.05	13.2
E	Wind waves	4.74	17.7
	1st swell partition	12.28	55.0
	2nd swell partition	7.89	20.1
	3rd swell partition	7.47	7.2

3.3.2. Combining Results From the Empirical and the Numerical Model

Combining insights from the empirical, process-based CERC method and the numerical BOSZ model reveals a constant sediment supply from the southern reef toward the island. Wave-induced currents transport the sediment around the island toward the island's lee side in the north. Throughout the dry season, sediment accumulates along Geiymiskih beach and at the southern end of Thoondu. Afterwards, in the wet season, the Thoondu spit forms at the northeastern end of Fuvahmulah (**Figure 4**). This formation can be elucidated with the CERC-formulation (**Figures 7**, **8**): In the wet season, the energy flux at the northern Geiymiskih beach carries sediment toward the east. At the same time, the swell dominated longshore energy flux is directed toward the north on Thoondu beach. Together, these hydrodynamic drivers transport sediment toward the north eastern headland of the island, forming the sand spit Thoondu. Inhabitants report and satellite images confirm that location and shape of the spit varies within the wet season (see **Supplementary Material**). The CERC-formulation is able to capture these changes when regarding the underlying hydrodynamic events (**Figure 9**). For example: The CERC-formulation is able to use the ERA5 climate data to explain singularities, such as those experienced on Fuvahmulah in the second half of the 2019 wet season. In September 2019, an anomaly occurred, where swell waves approached the island from $\theta_p \leq 135°$, leading to large transport rates in the CERC-equation: The highest longshore transport rate $q_{y,\max} = 8.98\,m^3\,h^{-1}$ came from swell waves with $H_s = 1.22\,m$ and $\theta_{\perp} = 79.9°$. This event is likely connected to a distinct temperature difference between the tropical eastern and western Indian Ocean, the IOD (Saji and Yamagata, 2003). The wave climate led to a beach protrusion on the edge of Geiymiskih to Thoondu beach and was well-appreciated by locals and tourists (see **Supplementary Material**). After the Thoondu spit formed in the wet season, the dry season wave climate leads to sediment depletion of the Thoondu spit, while new sediment accumulations form on Geiymiskih and Thoondu beach.

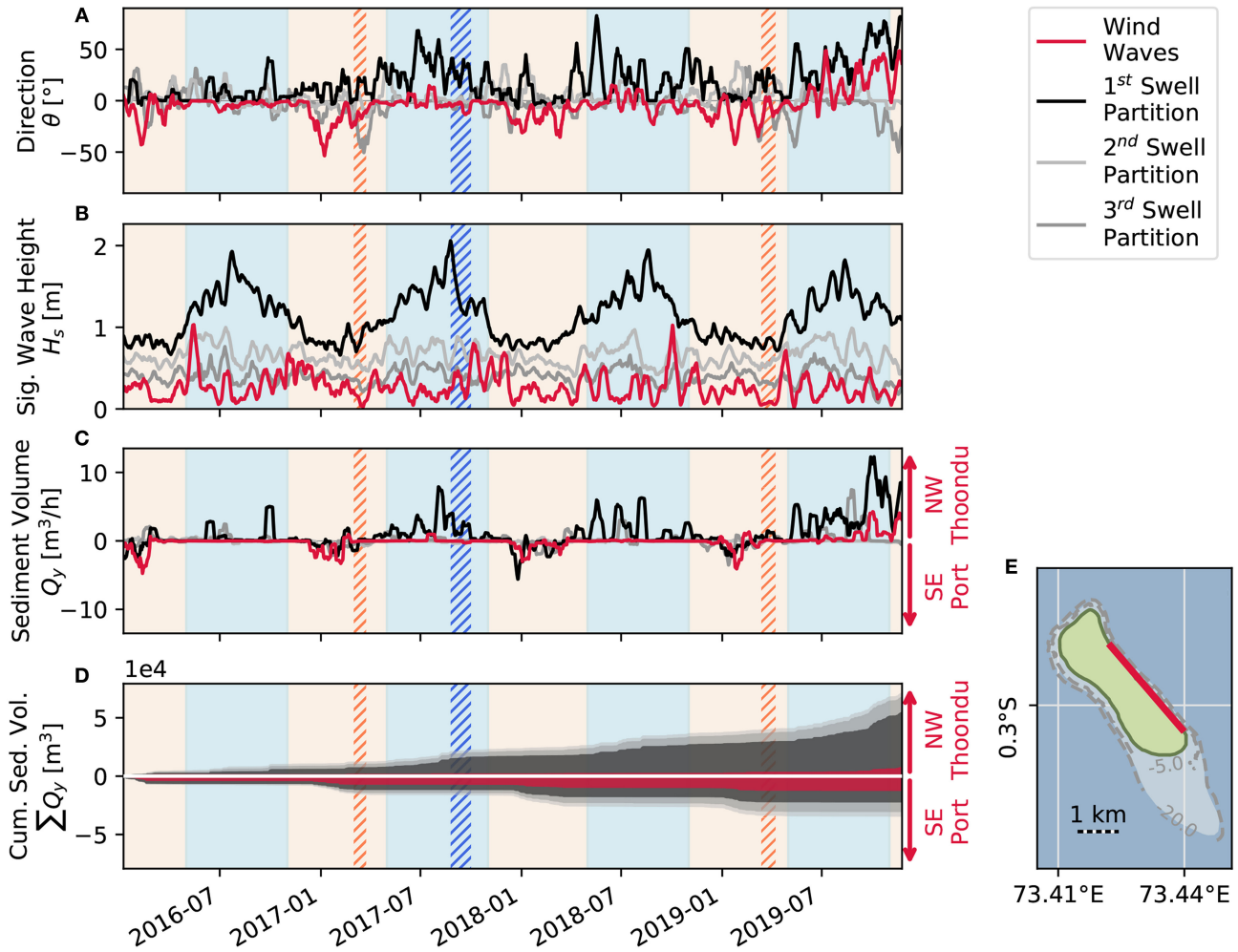

FIGURE 8 | (A) Averaged incident wave direction $\theta_{\perp,wp}$, measured as difference from the coastline normal $\alpha_{\perp}$ and **(B)** wave height $H_{s,wp}$ of each wave partition *wp* used for **(C)** longshore sediment transport rates $q_{y,wp}$ and **(D)** cumulative sediment volume $Q_{y,wp}$, transported alongshore the, marked with an crimson line on the map **(E)**. The crimson line is accordance with the crimson line in **Figure 6** (see **Table 3** for corresponding peak transport rate values $q_{y,max}$ and the contribution of each wave partition to Q_y). The time series shows values from January 2016 to November 2019. Negative values for $q_{y,wp}$ and $Q_{y,wp}$ indicate a transport toward the seaport in the southeast, while positive values lead to sediment transport toward Thoondu beach in the northwest. The time series shows the dry season with orange and the wet season with blue background. Field campaign 1 and 3 (orange hatched area) took place in March 2017 and 2019. Field campaign 2 (blue hatched area) was conducted in September 2017.

4. DISCUSSION

Sediment distribution on a reef is subject to (a) hydrodynamic forcing, for example by waves, wave transformation and tides, (b) the reef shape and bathymetry, defining wave propagation and thus current direction on the reef platform, as well as (c) sediment supply of the reef. This study used wave data from the climate reanalysis model ERA5 in the process-based, empirical CERC method and the phase-resolving, depth-integrated numerical model BOSZ to study the associated morphodynamic response on the Maldivian reef island Fuvahmulah. On this basis, the study linked these insights to comprehend measured shoreline changes on the island's beaches and the seasonal formation of the sand spit Thoondu in the north of the island.

As climate data resources have been scarce and of lower resolution, former studies usually combined significant wave heights H_s of wind waves and swell, but ignored their misalignment (Hildebrandt et al., 2019). This procedure emphasizes the dominant components but neglects the local characteristics. But the availability and constant improvement of climate reanalysis models provide more detailed boundary conditions today. The ocean wave model of ERA5 uses the wind input provided by their climate data set. However, the ERA5 wind data tends to result in underestimated significant wave heights. But compared to earlier releases of ECMWF's climate reanalysis models, the latest release of ECMWF's climate reanalysis model ERA5 improves the spatio-temporal resolution of it's predecessors with a 0.25° spatial resolution in latitudinal

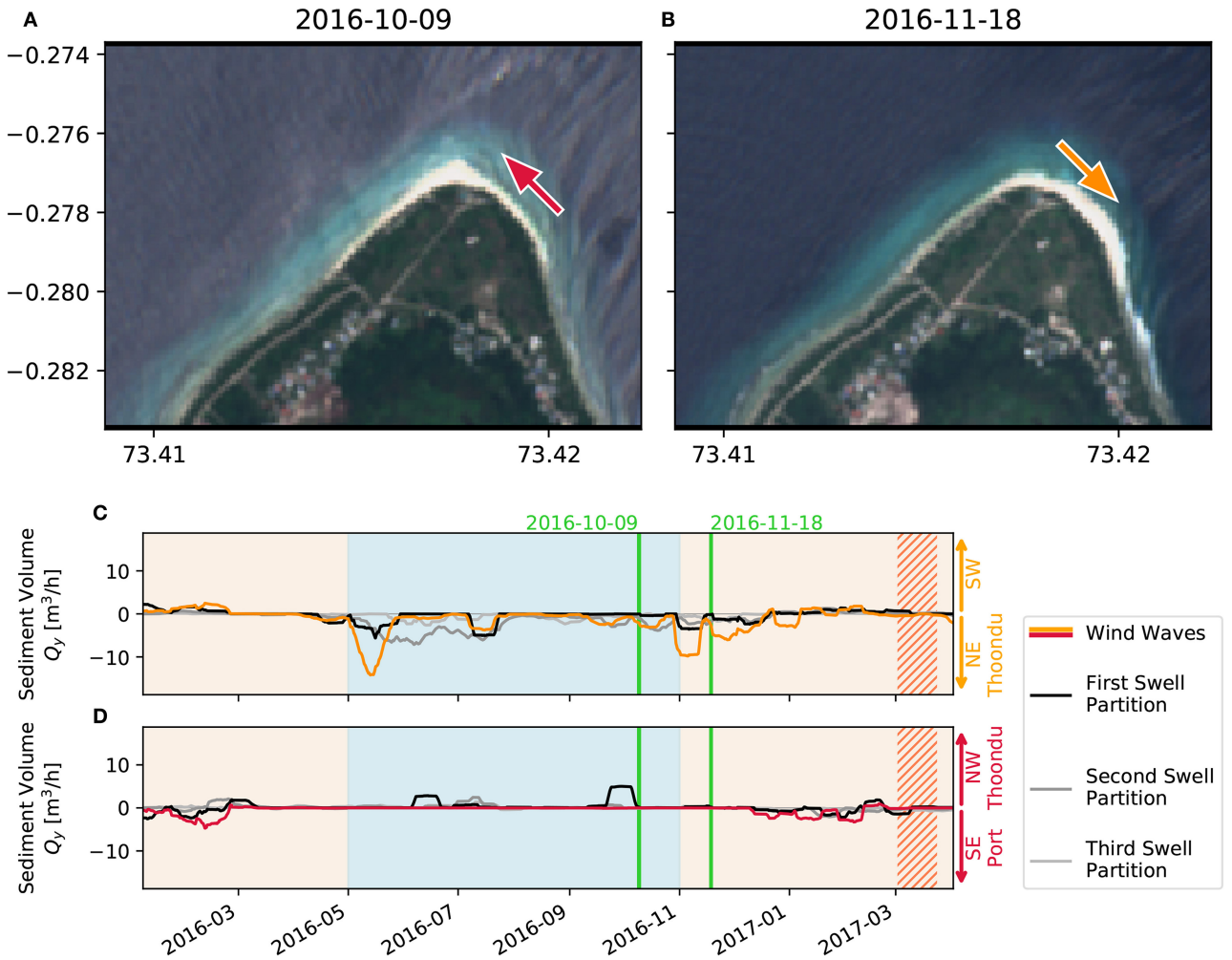

FIGURE 9 | Sentinel satellite images of northern Fuvahmulah on October 9, 2016 **(A)** and November 28, 2016 **(B)** and longshore sediment transport on Thoondu **(C)** and Geiymiskih Fannu beach **(D)** at the associated time of the satellite images (green line). **(C,D)** Show zoomed data from the longshore sediment transport rates $q_{y,wp}$ (**Figures 7**, **8**). The orange hatched area shows the time of the first field campaign for this study. The satellite images contain Copernicus Sentinel data, accessed through EO Browser (true color, red green blue).

and longitudinal direction and hourly temporal resolution (C3S, 2017). The hourly resolution of the current, publicly available model ERA5 improves the computation of significant wave heights and successfully reduces errors—especially in extreme events (Wiese et al., 2018). These factors—the good spatio-temporal data availability and trustworthy reconstruction of the wave climate—facilitate event based hind- and forecasting in the CERC formulation. On the other hand, the sheer amount of wave data results in a challenging number of feasible and reasonable numerical simulations. To tackle this challenge, this study combines the empirical CERC-formulation with information of a numerical model, calculating wave-induced currents approaching Fuvahmulah from the dominant wave directions:

The CERC-formulation is a common tool to estimate longshore sediment transport on sandy beaches (CERC, 1984; Schoonees and Theron, 1995) and works best for site-specific adaptation of the empirical coefficient K (Smith et al., 2009). It is able to process the high resolution data of the ERA5 data set. But application of the CERC-formulation for calcareous sediments and on coral reef islands has been rare (for example in Shope and Storlazzi, 2019). Its simplicity omit more complex sediment transport processes (van Rijn, 2005; Shope and Storlazzi, 2019) having an impact on each component of the CERC-equation $q_y = P_y \cdot I_y$:

The sediment transport rate q_y itself focuses on longshore sediment distribution but gives no information on cross-shore beach response (Atkinson et al., 2018) or cross-shore transport components. Therefore, the CERC-approach cannot estimate sediment transport toward the island and thus, for example, the role of the southern Fuvahmulah reef as sediment source.

The wave energy flux P_y captures the wave energy component of coastal longshore transport. Albeit the CERC-equation always includes at least one parameter at the breaker line, waves

transform differently when propagating over milder sloping sandy beaches compared to typical reef bathymetries with steep reef fronts followed by near horizontal reef flats. Furthermore, the wave energy flux P_y is based on the significant wave height H_s, but does not consider water level undulations on sub- and intratidal timescales (Pomeroy et al., 2018), sediment transport mechanisms by low-frequency waves and reef flat resonances (Roeber and Bricker, 2015; Cheriton et al., 2016; Gawehn et al., 2016), or other hydrodynamic effects on smaller scales, such as atoll lagoon flushing by wave pumping and gravity draining (Gourlay and Colleter, 2005; Callaghan et al., 2006).

Applying the sediment component I_y of the CERC equation for complex reef bathymetries requires an improved understanding over sandy or rocky bottoms. However, as of today, sediment transport over reef bottoms is still subject to current research (Pomeroy et al., 2015; Ryan et al., 2019). Moreover, while sediment mobility under waves is well-described for sandy marine aggregates (Turner and Masselink, 1998; Nielsen et al., 2001), wave-induced transport processes differ for coarser sediments (van Rijn, 2005; Austin and Masselink, 2006). The present study advances the application of the CERC-formulation on reef islands by combining measured data with insights of numerically modeled hydrodynamics, but further research is required to achieve a more sensible estimation of the empirical coefficient K for calcareous sediment volumes on coral reef islands—for example with measured sediment data on the scale of several single wave events. As sediment volumes from the CERC-equation are sensible to K, the results presented in this study (**Figures 7–9** and **Table 3**) must be interpreted as approximations of wave-induced morphodynamic processes rather than providing exact real-world sediment volumes (which is in accordance with the procedure of Shope and Storlazzi, 2019). For example: when considering the measured volumes in dry season 2017 instead of 2019, estimations of K—and thus calculated volumes—would vary by a factor of about $\pm \sim 3$.
Albeit each component q_y, P_y and I_y of the CERC-formulation underlies limitations, the equation is able to calculate longshore energy flux and corresponding sediment transport on different time scales. The results show that with highly resolved, multi-directional wave input, it can capture both the seasonal Thoondu spit formation as well as the beach formation initiated by an IOD-event in late wet season 2019 (see **Figure 9**).

When comparing the empirical with a numerical approach, the numerical approach can deliver more details on the hydrodynamic background of sediment transport: The depth-averaged hydrodynamic model indicates a more complex effect of the wave-induced current pattern near the beaches than given by the CERC method (**Figure 5**). In general, the numerical model confirms the directional components calculated with the CERC formulation (**Figure 5**). However, in the CERC formulation, waves from $\theta_p = 135^\circ$ (**Figure 5B**) would have a high influence ($\theta_\perp \sim \pm 45^\circ$) on the southern beaches, but a low influence on the east side ($\theta_\perp \sim +9^\circ$). On the contrary, the numerical model shows that wave-induced current velocities on the east and south side are in the same order of magnitude (about 1–2 m s^{-1}). A similar discrepancy can be seen on the west side for swell wave components with $\theta_p = 157^\circ$ (**Figure 5C**), inducing high currents in the numerical model, but having lower significance in the CERC-method ($\theta_\perp \sim 17^\circ$). But the $\theta_p = 202^\circ$ component shows the most significant difference: while the CERC-method calculates an upward directed sediment rate ($\theta_\perp \sim 45^\circ$) in front of the airport at the southwest side of Fuvahmulah, the current pattern of the numerical model depict a southeast ward directed current (**Figure 5D**). The numerical models also disclose an influence of south to southeastern swells on the lee-side of the island, but these are outside the northern beaches' incident wave direction range $\theta_\perp$ of −90–90° and thus remain unconsidered in the CERC-equation.

Even though numerical approaches are able to capture the hydrodynamics in reef environments (Roeber and Bricker, 2015; Masselink et al., 2019), implementation of morphodynamic changes into phase-resolving wave models is challenging (McCall et al., 2014). Here, the numerical model only shows depth-integrated flow velocities on the reef and not the altered velocity profile by the reef structure. Further research is required on the interaction of calcareous sediment and reef-island hydrodynamics in numerical models to extract more reliable and robust sediment transport rates and volumes. In the frame of this work, numerical models can only indicate sediment transport potential via wave-induced current velocity. While the results from this study illustrate that sediment transport on reef scale can be well-explained with ocean wave forcing, other studies on beach scale found further factors influencing sediment distribution—for example the complexity and roughness of reef structures and their role for hydrodynamic flow (Callaghan et al., 2006) and sediment transport (Pomeroy et al., 2015; Shope and Storlazzi, 2019) or wind-stresses and varying water levels due to sea-level rise or tides (Pomeroy et al., 2017, 2018; Atkinson et al., 2018). In the case of Fuvahmulah however, with a maximum tidal range of 1.1 m, currents from tides and ocean circulation are of minor importance, as they are about an order of magnitude below wave-induced currents (David et al., 2019). The insights from the numerical model complement the findings of the CERC-method and put the measured morphological changes into an hydrodynamic context.

The transported sediment is visible in form of sediment on the coastline of the island. In this study, UAVs recorded sediment volumes, being reconstructed by means of structure from motion (SfM). The first two campaigns were referred to the DEMs of the third campaign via vGCPs of unique natural or structural features. This approach still yields reasonably good results, but contains higher errors in the photogrammetric process than recording unique GCPs for each flight in each campaign (see **Supplementary Material**). Therefore, it should only be applied if no individual GCPs for each campaign are available—as in this case. Especially areas with deteriorated visibility can make vGCP identification and point cloud reconstruction challenging. An example are vegetated areas or areas submerged by water or sand. The results of this study however encourage the use of UAV-borne data recorded even in subpar field conditions, as they remain valuable data with useful information. In this study, errors of the DEMs aligned with vGCPs are still within the upper range of expectable errors in UAV-based photogrammetry (Casella et al., 2020).

The overview of the resulting sediment budget (**Figure 3**) is presented in volume over dry beach area. Some challenges remain by measuring volumetric sediment changes by means of UAV-borne photogrammetry, such as beach access and underwater areas. This study uses the volume over dry beach method consistently for the overview, but defines interpolation nodes on the submerged reef between the last dry point of the reef in one season and the associated dry beach point in the other season for the northern beaches Geiymiskih and Thoondu northwest. Otherwise, large volumes of the northern beaches would remain unspecified. The error of defining the coordinates of the interpolation nodes is within the error range of the photogrammetric process. The interpolation of wet season beaches at Thoondu north depends on estimated reef depths derived from orthophotos and reef depths of adjacent beaches and can contain errors in decimeter scale. The interpolation between two nodes on the reef neglects the bottom roughness of the beach and thus introduces further inaccuracies to the volumes. With sediment volumes in the order of $\mathcal{O}(4-5)$ cubic meters, the total influence of these simplifications is however minor. Also, erosion due to coastal infrastructure is in the order of (cubic-) decimeters and rather affects the consolidated material of the coast of Fuvahmulah (David et al., 2019) than the bulk sediment evaluated with the volume over dry beach method. Thus, erosion must be studied on a different scale.

Sediment supply depends on the location of corals on the reef (Ryan et al., 2019) and coral type (Hamylton et al., 2017). Gross and net production as well as bio-erosion of calcium carbonate are site specific and depend on different environmental factors. In general, reef island formation is based on the fact that the coral reef produces calcium carbonate, which erodes and is transported over the reef (Mandlier and Kench, 2012). Insufficient sediment supply can have several impacts: coasts retreat depending on their orientation toward the dominant incident wave direction, reef island positions on an atoll varies (Shope and Storlazzi, 2019), or islands disappear as net sediment accretion cannot keep up with sea level rise (Albert et al., 2016). With sufficient sediment supply and without artificial interference, the coastline of reef islands is meant to be stable (Kench, 2012). This study does not provide a specific sediment production budget for Fuvahmulah, but uses the bio-erosion estimates of $3.4 \pm 0.4\,\mathrm{kg\,CaCO_3\,m^{-2}\,yr^{-1}}$ from an island on the neighboring atoll (Ryan et al., 2019). Here, *"the upper reef* [platform] *surface act*[s] *as the carbonate factory for islands"* (Ryan et al., 2019). Despite the regional proximity and similarities of both reefs, total carbonate production rate of the reef depends on several factors, such as the eco-geomorphological zones on the reef platform (Hamylton et al., 2017; Ryan et al., 2019), having an influence on the bio-erosion rate and thus on the calculations in this study.

While the west side of Fuvahmulah is stable, the port construction blocks the sediment transport and leads to sand accumulation in the south of the island in front of the port, as well as slow, but substantial erosion on the port's lee side in the southeast of the island. This erosion becomes visible in examinations on smaller scales and epitomizes a disturbance of natural systems by anthropogenic interventions (the port's impact on the southcoast of Fuvahmulah was analyzed in David et al., 2019). On the other hand, the sediment budgets verify sediment produced on the reef migrates around the island to the lee-side of Fuvahmulah. Then, the final destination of the sediment is are the northern beaches Thoondu and Geiymiskih. Here, a sediment volume deficit from wet to dry season indicates sediment moving off the reef plateau, especially since volume changes at adjacent beaches are low. The positive sediment budget between dry season 2017 and 2019 support the thesis of reef recovery in the region after the 2016 reef bleaching event (Ryan et al., 2019).

5. CONCLUSION

Ocean climate pressures influence sediment production and distribution pathways on the reef. The dynamic reef island morphology is a natural response to changing impacts. Within reef island environments however, sustainable, low-regret coastal development requires an understanding of the underlying processes of island morphology.

The present study deals with the fringing reef island Fuvahmulah on the Maldives. Based on three field campaigns, UAV-based photogrammetry revealed intra- and interannual changes of sediment volumes and coastlines. The coastline of the island was separated into morphological cells showing that the lateral coastlines on the west and east of the elliptical island are mostly stable. Only on the southeastern coast above the seaport, Fuvahmulah experiences erosion, which becomes measurable at a lower scale (David et al., 2019). In contrast, the lee-side in the north of Fuvahmulah has a highly active morphology, where beach face and location change even within the seasons. The general morphological pattern on the northern headland is characterized by typical seasonal sediment depots on Geiymiskih and Thoondu beach in the dry season. In the wet season the sediment moves to the northern tip of Fuvahmulah, where the Thoondu spit is formed. This natural feature makes the beach very popular and is highly valued by the community and considered a landmark of the island (Ratter et al., 2019).

Morphological changes on the reef are triggered by hydrodynamic forcing. Therefore, this study exploits hourly climate reanalysis model wave data to quantify longshore sediment distribution around the island with the CERC method. Dominant south to southeasterly swells are characteristic for the regional Maldivian hydrodynamic regime (Kench and Brander, 2006; Kench and Mann, 2017). These swells induce a constant sediment supply from the southeastern reef plateau. The sediment stream goes around the lateral sides of Fuvahmulah to the northern headland, where the Thoondu spit forms in the wet season. Local wind-wave and subordinate swell events shape the northern beaches within the seasons.

By adapting and validating the empirical coefficient K with the measurements from the field campaigns, the CERC formulation is capable of capturing morphodynamic changes after hydrodynamic events. This method facilitates processing the high resolution wave data from the climate data models for quantitative hind- and forecast of longshore sediment

transport. Numerical methods give supplementary insights beyond the empirical CERC approach and hence a more holistic view on the complex hydrodynamic background of the reef for certain combinations of dominant wave parameters or single events. However, further advances in numerical models are required to directly couple hydrodynamic drivers and morphodynamic response on reef islands and calcareous sediment.

This study shows that seasonal wave climate and associated, wave-induced currents can explain the formation of local characteristic beach phenomena like the Thoondu spit. On annual timescales the seasonally dynamic morphology stabilizes the island's shoreline analogous to beach nourishment on sandy beaches. This study presented coastal engineering methods to exploit publicly available climate reanalysis data in high-resolution to assess the site-specific influence of hydrodynamic drivers on reef island morphology. Even though erosion on Fuvahmulah has to be studied on a different scale (David et al., 2019), sediment trajectories reveal locations with increased erosion potential on the lee-side of disturbances in the natural sediment stream. Because anthropogenic interventions into the natural dynamics disturb the natural ability to respond to ocean climate pressures the design of coastal infrastructure on low-lying reef islands must include an assessment of reef islands' natural beach nourishment potential to avoid interference before taking action. With this, reef island communities can reduce shoreline erosion, improve their resilience and decrease their risk to suffer from sea level rise and associated impacts.

DATA AVAILABILITY STATEMENT

The field data supporting the findings of this study are available from the corresponding author upon reasonable request. Wave climate data is available from the Copernicus Climate Change Service (C3S, 2017). Satellite images from Copernicus Sentinel data were accessed through the EO Browser.

AUTHOR CONTRIBUTIONS

CD conducted the field campaign, research, analysis, and wrote the manuscript with input from TS. TS (co-)designed the research project, provided guidance, edited, and contributed to the final manuscript. All authors contributed to the article and approved the submitted version.

FUNDING

This study took place in the project Dealing with change in SIDS: societal action and political reaction in sea level change adaptation in Small Island Developing States (DICES), grant no. SCHL 503/17-1. The project was framed within the priority program (SPP 1889) 'Regional Sea Level Change and Society' (SeaLevel, see www.spp-sealevel.de) of the German Research Foundation (Deutsche Forschungsgemeinschaft, DFG). The publication of this article was funded by the Open Access fund of Leibniz Universität Hannover.

ACKNOWLEDGMENTS

The authors would like to thank Ali Ahmed, Pablo Ballesteros, Tatiana Ivanova, René Klein, Nina Kohl, Manò Schütt, Ibrahim Shiyan (Panda), Zahid as well as Marion, and Uwe Zander for their help in the field campaigns. On the Maldives, the authors were supported by the Maldives Meteorological Service (MMS), Fuvahmulah Island Council, and Fuvahmulah DIVE School.

The authors further appreciate the involvement of the working group of Maike Paul for reviewing the manuscript. We further acknowledge the working group of Jan Visscher, Rik Gijsman, as well as our project members in DICES Susann Adloff, Arne Henning, Beate Ratter, and Katrin Rehdanz for their professional input.

Additionally the authors thank Volker Roeber and Jannek Gundlach for their feedback concerning numerical models as well as Jean Bidlot, Mark Hemer, and Todd Spindler for their help in accessing climate reanalysis data. Also, Elisa Casella and Alessio Rovere gave valuable insights and feedback to UAV-based photogrammetry, while Tobias Kersten helped with geodetic questions before the third field campaign and while post-processing.

SUPPLEMENTARY MATERIAL

The Supplementary Material for this article can be found online at: https://www.frontiersin.org/articles/10.3389/fmars.2020.538675/full#supplementary-material

REFERENCES

Albert, S., Leon, J. X., Grinham, A. R., Church, J. A., Gibbes, B. R., and Woodroffe, C. D. (2016). Interactions between sea-level rise and wave exposure on reef island dynamics in the Solomon Islands. *Environ. Res. Lett.* 11:054011. doi: 10.1088/1748-9326/11/5/054011

Andersson, A. (2015). A fundamental paradigm for coral reef carbonate sediment dissolution. *Front. Mar. Sci.* 2:52. doi: 10.3389/fmars.2015.00052

Atkinson, A. L., Baldock, T. E., Birrien, F., Callaghan, D. P., Nielsen, P., Beuzen, T., et al. (2018). Laboratory investigation of the bruun rule and beach response to sea level rise. *Coast. Eng.* 136, 183–202. doi: 10.1016/j.coastaleng.2018.03.003

Austin, M. J., and Masselink, G. (2006). Swash–groundwater interaction on a steep gravel beach. *Cont. Shelf Res.* 26, 2503–2519. doi: 10.1016/j.csr.2006.07.031

Bidlot, J.-R. (2016). *Ocean Wave Model Output Parameters*. Reading: European Centre for Medium-RangeWeather Forecasts (ECMWF).

Bosboom, J., and Stive, M. J. F. (2015). *Coastal Dynamics I, Volume 0.5*. Delft: Delft Academic Press.

Burcharth, H. F., Hawkins, S. J., Zanuttigh, B., and Lamberti, A. (2007). "Design tools related to engineering," in *Environmental Design Guidelines for Low Crested Coastal Structures, Chapter 13*, eds H. F. Burcharth, S. J. Hawkins, B. Zanuttigh, and A. Lamberti (Oxford: Elsevier Science Ltd), 203–333. doi: 10.1016/B978-008044951-7/50033-6

C3S (2017). *ERA5, Fifth Generation of ECMWF Atmospheric Reanalyses of the Global Climate by the Copernicus Climate Change Service (C3S)*. Copernicus Climate Change Service Climate Data Store (CDS). Available online at: https://cds.climate.copernicus.eu/cdsapp#!/home (accessed December 6, 2019).

Cai, W., Santoso, A., Wang, G., Weller, E., Wu, L., Ashok, K., et al. (2014). Increased frequency of extreme Indian Ocean Dipole events due to greenhouse warming. *Nature* 510, 254–258. doi: 10.1038/nature13327

Caldwell, P. C., Merrifield, M. A., and Thompson, P. R. (2015). *Sea level Measured by Tide Gauges From Global Oceans-The Joint Archive for Sea Level Holdings (NCEI Accession 0019568). Dataset. Version 5.5*. NOAA National Centers for Environmental Information.

Callaghan, D. P., Nielsen, P., Cartwright, N., Gourlay, M. R., and Baldock, T. E. (2006). Atoll lagoon flushing forced by waves. *Coast. Eng.* 53, 691–704. doi: 10.1016/j.coastaleng.2006.02.006

Casella, E., Collin, A., Harris, D., Ferse, S., Bejarano, S., Parravicini, V., et al. (2016). Mapping coral reefs using consumer-grade drones and structure from motion photogrammetry techniques. *Coral Reefs* 36, 269–275. doi: 10.1007/s00338-016-1522-0

Casella, E., Drechsel, J., Winter, C., Benninghoff, M., and Rovere, A. (2020). Accuracy of sand beach topography surveying by drones and photogrammetry. *Geomar. Lett.* 40, 255–268. doi: 10.1007/s00367-020-00638-8

CERC (1984). *Shore Protection Manual, Vol. 1*. Vicksburg, MS: Coastal Engineering Research Center (CERC), Department of the U.S. Army,Waterways Experiment Station, Corps of Engineers, Coastal Engineering Research Center.

Chave, K. E., Smith, S. V., and Roy, K. J. (1972). Carbonate production by coral reefs. *Mar. Geol.* 12, 123–140. doi: 10.1016/0025-3227(72)90024-2

Cheriton, O. M., Storlazzi, C. D., and Rosenberger, K. J. (2016). Observations of wave transformation over a fringing coral reef and the importance of low-frequency waves and offshore water levels to runup, overwash, and coastal flooding. *J. Geophys. Res. Oceans* 121, 3121–3140. doi: 10.1002/2015JC011231

Collins, M., Sutherland, M., Bouwer, L., Cheong, S.-M., Frlicher, T., Combes, H. J. D., et al. (in press). "Extremes, abrupt changes and managing risk," in *IPCC Special Report on the Ocean and Cryosphere in a Changing Climate*, eds H. O. Pörtner, D. Roberts, V. Masson-Delmotte, P. Zhai, M. Tignor, E. Poloczanska, et al., 589–655.

Dangendorf, S., Hay, C., Calafat, F. M., Marcos, M., Piecuch, C. G., Berk, K., et al. (2019). Persistent acceleration in global sea-level rise since the 1960s. *Nat. Clim. Change* 9, 705–710. doi: 10.1038/s41558-019-0531-8

David, C. G., Roeber, V., Goseberg, N., and Schlurmann, T. (2017). Generation and propagation of ship-borne waves–solutions from a Boussinesq-type model. *Coast. Eng.* 127, 170–187. doi: 10.1016/j.coastaleng.2017.07.001

David, C. G., Schlurmann, T., and Roeber, V. (2019). "Coastal Infrastructure on Reef Islands–the Port of Fuvahmulah, the Maldives as example of maladaptation to sea-level rise?" in *Coastal Structures 2019*, eds N. Goseberg and T. Schlurmann (Hannover: Bundesanstalt fr Wasserbau), 874–885.

David, C. G., Schulz, N., and Schlurmann, T. (2016). "Assessing the application potential of selected ecosystem-based, low-regret coastal protection measures," in *Ecosystem-Based Disaster Risk Reduction and Adaptation in Practice*, eds F. G. Renaud, K. Sudmeier-Rieux, M. Estrella, and U. Nehren (Cham: Springer International Publishing), 457–482. doi: 10.1007/978-3-319-43633-3_20

Duvat, V. K. E., and Magnan, A. K. (2019). Rapid human-driven undermining of atoll island capacity to adjust to ocean climate-related pressures. *Sci. Rep.* 9:15129. doi: 10.1038/s41598-019-51468-3

East, H. K., Perry, C. T., Kench, P. S., Liang, Y., and Gulliver, P. (2018). Coral reef island initiation and development under higher than present sea levels. *Geophys. Res. Lett.* 45, 11265–11274. doi: 10.1029/2018GL079589

Emanuel, K. (1988). The maximum intensity of hurricanes. *J. Atmos. Sci.* 45, 1143–1155. doi: 10.1175/1520-0469(1988)045<1143:TMIOH>2.0.CO;2

Ferrario, F., Beck, M. W., Storlazzi, C. D., Micheli, F., Shepard, C. C., and Airoldi, L. (2014). The effectiveness of coral reefs for coastal hazard risk reduction and adaptation. *Nat. Commun.* 5:3794. doi: 10.1038/ncomms4794

Gawehn, M., van Dongeren, A., van Rooijen, A., Storlazzi, C. D., Cheriton, O. M., and Reniers, A. (2016). Identification and classification of very low frequency waves on a coral reef flat. *J. Geophys. Res. Oceans* 121, 7560–7574. doi: 10.1002/2016JC011834

Gourlay, M. R., and Colleter, G. (2005). Wave-generated flow on coral reefs—an analysis for two-dimensional horizontal reef-tops with steep faces. *Coast. Eng.* 52, 353–387. doi: 10.1016/j.coastaleng.2004.11.007

Hamylton, S. M., Duce, S., Vila-Concejo, A., Roelfsema, C. M., Phinn, S. R., Carvalho, R. C., et al. (2017). Estimating regional coral reef calcium carbonate production from remotely sensed seafloor maps. *Rem. Sens. Environ.* 201, 88–98. doi: 10.1016/j.rse.2017.08.034

Hanson, J. L., and Phillips, O. M. (2001). Automated analysis of ocean surface directional wave spectra. *J. Atmos. Ocean. Technol.* 18, 277–293. doi: 10.1175/1520-0426(2001)018<0277:AAOOSD>2.0.CO;2

Harris, D. L., Rovere, A., Casella, E., Power, H., Canavesio, R., Collin, A., et al. (2018). Coral reef structural complexity provides important coastal protection from waves under rising sea levels. *Sci. Adv.* 4:eaao4350. doi: 10.1126/sciadv.aao4350

Hermes, J. C., Masumoto, Y., Beal, L. M., Roxy, M. K., Vialard, J., Andres, M., et al. (2019). A sustained ocean observing system in the Indian Ocean for climate related scientific knowledge and societal needs. *Front. Mar. Sci.* 6:355. doi: 10.3389/fmars.2019.00355

Hildebrandt, A., Schmidt, B., and Marx, S. (2019). Wind-wave misalignment and a combination method for direction-dependent extreme incidents. *Ocean Eng.* 180, 10–22. doi: 10.1016/j.oceaneng.2019.03.034

Horrillo, J., Grilli, S. T., Nicolsky, D., Roeber, V., and Zhang, J. (2014). Performance benchmarking tsunami models for NTHMP's inundation mapping activities. *Pure Appl. Geophys.* 172, 869–884. doi: 10.1007/s00024-014-0891-y

IPCC (2012). "Managing the risks of extreme events and disasters to advance climate change adaptation," in *A Special Report of Working Groups I and II of the Intergovernmental Panel on Climate Change (IPCC)*, eds C. B. Field, V. Barros, T. F. Stocker, Q. Dahe, D. J. Dokken, K. L. Ebi, et al. (Cambridge; New York, NY: Cambridge University Press), 582.

Kench, P. S. (2012). "Compromising Reef Island shoreline dynamics: legacies of the engineering paradigm in the Maldives," in *Pitfalls of Shoreline Stabilization: Selected Case Studies*, eds J. A. G. Cooper and O. H. Pilkey (Dordrecht: Springer Netherlands), 165–186. doi: 10.1007/978-94-007-4123-2_11

Kench, P. S., and Brander, R. W. (2006). Response of reef island shorelines to seasonal climate oscillations: South Maalhosmadulu atoll, Maldives. *J. Geophys. Res. Earth Surf.* 111. doi: 10.1029/2005JF000323

Kench, P. S., and Mann, T. (2017). Reef Island evolution and dynamics: insights from the Indian and Pacific Oceans and perspectives for the Spermonde Archipelago. *Front. Mar. Sci.* 4:145. doi: 10.3389/fmars.2017.00145

Kumar, P., Kaur, S., Weller, E., and Min, S.-K. (2019). Influence of natural climate variability on the extreme ocean surface wave heights over the Indian Ocean. *J. Geophys. Res. Oceans* 124, 6176–6199. doi: 10.1029/2019JC015391

Longuet-Higgins, M. S. (1970). Longshore currents generated by obliquely incident sea waves: 2. *J. Geophys. Res.* 75, 6790–6801. doi: 10.1029/JC075i033p06790

Lynett, P. J., Gately, K., Wilson, R., Montoya, L., Arcas, D., Aytore, B., et al. (2017). Inter-model analysis of tsunami-induced coastal currents. *Ocean Modell.* 114, 14–32. doi: 10.1016/j.ocemod.2017.04.003

Magnan, A., Garschagen, M., Gattuso, J. P., Hay, J. E., Hilmi, N., Holland, E., et al. (in press). "Integrative cross-chapter box on low-lying islands and coasts," in *Special Report on Ocean and Cryosphere in a Changing Climate*, eds H. O. Pörtner, D. Roberts, V. Masson-Delmotte, P. Zhai, M. Tignor, E. Poloczanska, et al., 657–674.

Mandlier, P. G., and Kench, P. S. (2012). Analytical modelling of wave refraction and convergence on coral reef platforms: implications for island formation and stability. *Geomorphology* 159–160, 84–92. doi: 10.1016/j.geomorph.2012.03.007

Masselink, G., Tuck, M., McCall, R., van Dongeren, A., Ford, M., and Kench, P. (2019). Physical and numerical modeling of infragravity wave generation and transformation on coral reef platforms. *J. Geophys. Res. Oceans* 124, 1410–1433. doi: 10.1029/2018JC014411

McCall, R., Masselink, G., Poate, T., Roelvink, J., Almeida, L., Davidson, M., et al. (2014). Modelling storm hydrodynamics on gravel beaches with XBeach-G. *Coast. Eng.* 91, 231–250. doi: 10.1016/j.coastaleng.2014.06.007

McLean, R., and Kench, P. (2015). Destruction or persistence of coral atoll islands in the face of 20th and 21st century sea-level rise? *Wiley Interdiscipl. Rev. Clim. Change* 6, 445–463. doi: 10.1002/wcc.350

MEE (2014). *Environment & Social Assessment & Management Framework–Climate Change Adaptation Project*. Technical report, Ministry of Environment and Energy. Available online at: http://documents.worldbank.org/curated/en/939971468329099370/pdf/E47010SAR0EA0P1533010Box385392B00PUBLIC0.pdf (accessed December 27, 2019).

Möller, I., Kudella, M., Rupprecht, F., Spencer, T., Paul, M., van Wesenbeeck, B. K., et al. (2014). Wave attenuation over coastal salt marshes under storm surge conditions. *Nat. Geosci.* 7, 727–731. doi: 10.1038/ngeo2251

Naeem, H. (2006). *Foahmulaku Beach Erosion Survey & Coastal Protection Report*. Technical Report. Malé: Ministry of Environment, Energy and Water.

Narayan, S., Beck, M. W., Reguero, B. G., Losada, I. J., van Wesenbeeck, B., Pontee, N., et al. (2016). The effectiveness, costs and coastal protection benefits of natural and nature-based defences. *PLoS ONE* 11:e154735. doi: 10.1371/journal.pone.0154735

Nielsen, P., Robert, S., Mller-Christiansen, B., and Oliva, P. (2001). Infiltration effects on sediment mobility under waves. *Coast. Eng.* 42, 105–114. doi: 10.1016/S0378-3839(00)00051-X

Nurse, L. A., McLean, R. F., Agard, J., Briguglio, L. P., Duvat-Magnan, V., Pelesikoti, N., et al. (2014). "Small islands," in *Climate Change 2014, Impacts, Adaptation, and Vulnerability. Part B: Regional Aspects. Contribution of Working Group II to the Fifth Assessment Report of the Intergovernmental Panel of Climate Change*, eds V. R. Barros, C. B. Field, D. J. Dokken, M. D. Mastrandrea, K. J. Mach, T. E. Bilir, et al. (Cambridge; New York, NY: Cambridge University Press), 1613–1654.

Oppenheimer, M., Glavovic, B., Hinkel, J., van de Wal, R., Magnan, A. K., Abd-Elgawad, A., et al. (in press). "Sea Level rise and implications for low lying islands, coasts and communities," in *IPCC Special Report on the Ocean and Cryosphere in a Changing Climate*, eds H. O. Portner, D. Roberts, V. Masson-Delmotte, P. Zhai, M. Tignor, E. Poloczanska, et al., 702.

Paul, M., and Gillis, L. (2015). Let it flow: how does an underlying current affect wave propagation over a natural seagrass meadow? *Mar. Ecol. Prog. Ser.* 523, 57–70. doi: 10.3354/meps11162

Perry, C. T., Alvarez-Filip, L., Graham, N. A. J., Mumby, P. J., Wilson, S. K., Kench, P. S., et al. (2018). Loss of coral reef growth capacity to track future increases in sea level. *Nature* 558, 396–400. doi: 10.1038/s41586-018-0194-z

Perry, C. T., Kench, P. S., Smithers, S. G., Riegl, B., Yamano, H., and Leary, M. J. O. (2011). Implications of reef ecosystem change for the stability and maintenance of coral reef islands. *Glob. Change Biol.* 17, 3679–3696. doi: 10.1111/j.1365-2486.2011.02523.x

Pisapia, C., Burn, D., and Pratchett, M. S. (2019). Changes in the population and community structure of corals during recent disturbances (February 2016–October 2017) on Maldivian coral reefs. *Sci. Rep.* 9:8402. doi: 10.1038/s41598-019-44809-9

Pomeroy, A. W., Lowe, R. J., Dongeren, A. R. V., Ghisalberti, M., Bodde, W., and Roelvink, D. (2015). Spectral wave-driven sediment transport across a fringing reef. *Coast. Eng.* 98, 78–94. doi: 10.1016/j.coastaleng.2015.01.005

Pomeroy, A. W. M., Lowe, R. J., Ghisalberti, M., Storlazzi, C., Symonds, G., and Roelvink, D. (2017). Sediment transport in the presence of large reef bottom roughness. *J. Geophys. Res. Oceans* 122, 1347–1368. doi: 10.1002/2016JC011755

Pomeroy, A. W. M., Lowe, R. J., Ghisalberti, M., Winter, G., Storlazzi, C., and Cuttler, M. (2018). Spatial variability of sediment transport processes over intratidal and subtidal timescales within a fringing coral reef system. *J. Geophys. Res. Earth Surf.* 123, 1013–1034. doi: 10.1002/2017JF004468

Ratter, B., Hennig, A., and Zahid (2019). Challenges for shared responsibility–political and social framing of coastal protection transformation in the Maldives. *Die Erde J. Geograph. Soc. Berlin* 150, 169–183. doi: 10.12854/erde-2019-426

Roeber, V., and Bricker, J. D. (2015). Destructive tsunami-like wave generated by surf beat over a coral reef during Typhoon Haiyan. *Nat. Commun.* 6:7854. doi: 10.1038/ncomms8854

Roeber, V., and Cheung, K. F. (2012). Boussinesq-type model for energetic breaking waves in fringing reef environments. *Coast. Eng.* 70, 1–20. doi: 10.1016/j.coastaleng.2012.06.001

Roeber, V., Cheung, K. F., and Kobayashi, M. H. (2010). Shock-capturing Boussinesq-type model for nearshore wave processes. *Coast. Eng.* 57, 407–423. doi: 10.1016/j.coastaleng.2009.11.007

Rutten, J., Ruessink, B. G., and Price, T. D. (2017). Observations on sandbar behaviour along a man-made curved coast. *Earth Surf. Process. Landf.* 43, 134–149. doi: 10.1002/esp.4158

Ryan, E. J., Hanmer, K., and Kench, P. S. (2019). Massive corals maintain a positive carbonate budget of a Maldivian upper reef platform despite major bleaching event. *Sci. Rep.* 9:6515. doi: 10.1038/s41598-019-42985-2

Saji, N., and Yamagata, T. (2003). Possible impacts of Indian Ocean Dipole mode events on global climate. *Clim. Res.* 25, 151–169. doi: 10.3354/cr025151

Saji, N. H., Goswami, B. N., Vinayachandran, P. N., and Yamagata, T. (1999). A dipole mode in the tropical Indian Ocean. *Nature* 401, 360–363. doi: 10.1038/43854

Schoonees, J. S., and Theron, A. K. (1995). *Accuracy and Applicability of the SPM Longshore Transport Formula, Chapter 188*. Kobe: American Society of Civil Engineers.

Schoonees, T., Mancheño, A. G., Scheres, B., Bouma, T. J., Silva, R., Schlurmann, T., et al. (2019). Hard structures for coastal protection, towards greener designs. *Estuar. Coasts* 42, 1709–1729. doi: 10.1007/s12237-019-00551-z

Shope, J. B., and Storlazzi, C. D. (2019). Assessing morphologic controls on Atoll Island alongshore sediment transport gradients due to future sea-level rise. *Front. Mar. Sci.* 6:245. doi: 10.3389/fmars.2019.00245

Skirving, W. J., Heron, S. F., Marsh, B. L., Liu, G., De La Cour, J. L., Geiger, E. F., et al. (2019). The relentless march of mass coral bleaching: a global perspective of changing heat stress. *Coral Reefs* 38, 547–557. doi: 10.1007/s00338-019-01799-4

Smith, E. R., Wang, P., Ebersole, B. A., and Zhang, J. (2009). Dependence of total longshore sediment transport rates on incident wave parameters and breaker type. *J. Coast. Res.* 2009, 675–683. doi: 10.2112/07-0919.1

Stive, M. J., de Schipper, M. A., Luijendijk, A. P., Aarninkhof, S. G., van Gelder-Maas, C., van Thiel de Vries, J. S., et al. (2013). A new alternative to saving our beaches from sea-level rise: the sand engine. *J. Coast. Res.* 2013, 1001–1008. doi: 10.2112/JCOASTRES-D-13-00070.1

Storlazzi, C. D., Elias, E. P., and Berkowitz, P. (2015). Many Atolls may be uninhabitable within decades due to climate change. *Sci. Rep.* 5:14546. doi: 10.1038/srep14546

Storlazzi, C. D., Gingerich, S. B., van Dongeren, A., Cheriton, O. M., Swarzenski, P. W., Quataert, E., et al. (2018). Most atolls will be uninhabitable by the mid-21st century because of sea-level rise exacerbating wave-driven flooding. *Sci. Adv.* 4:eaap9741. doi: 10.1126/sciadv.aap9741

Temmerman, S., Meire, P., Bouma, T. J., Herman, P. M. J., Ysebaert, T., and Vriend, H. J. D. (2013). Ecosystem-based coastal defence in the face of global change. *Nature* 504, 79–83. doi: 10.1038/nature12859

Tessler, Z. D., Vörösmarty, C. J., Grossberg, M., Gladkova, I., Aizenman, H., Syvitski, J. P. M., et al. (2015). Profiling risk and sustainability in coastal deltas of the world. *Science* 349, 638–643. doi: 10.1126/science.aab3574

Tory, K. J., and Frank, W. M. (2010). "Tropical cyclone formation," in *Global Perspectives on Tropical Cyclones* (San Jose, CA: World Scientific Publishing), 55–91. doi: 10.1142/7597

Turner, I. L., and Masselink, G. (1998). Swash infiltration-exfiltration and sediment transport. *J. Geophys. Res. Oceans* 103, 30813–30824. doi: 10.1029/98JC02606

van Rijn, L. C. (2005). *Principles of Sedimentation and Erosion Engineering in Rivers, Estuaries and Coastal Seas*. Amsterdam: Aqua Publications.

Wessel, P., and Luis, J. F. (2017). The GMT/MATLAB toolbox. *Geochem. Geophys. Geosyst.* 18, 811–823. doi: 10.1002/2016GC006723

Wiese, A., Staneva, J., Schulz-Stellenfleth, J., Behrens, A., Fenoglio-Marc, L., and Bidlot, J.-R. (2018). Synergy of wind wave model simulations and satellite observations during extreme events. *Ocean Sci.* 14, 1503–1521. doi: 10.5194/os-14-1503-2018

Wing, M. G., Eklund, A., and Kellogg, L. D. (2005). Consumer-grade global positioning system (GPS) accuracy and reliability. *J. Forestry* 103, 169–173. doi: 10.1093/jof/103.4.169

Woodroffe, C., McLean, R., Smithers, S., and Lawson, E. (1999). Atoll reef-island formation and response to sea-level change: West Island, Cocos (Keeling) Islands. *Mar. Geol.* 160, 85–104. doi: 10.1016/S0025-3227(99)00009-2

Conflict of Interest: The authors declare that the research was conducted in the absence of any commercial or financial relationships that could be construed as a potential conflict of interest.